

Robust Foreground-Background Separation for Severely-Degraded Videos Using Convolutional Sparse Representation Modeling

Kazuki Naganuma, *Member, IEEE*, Shunsuke Ono, *Senior Member, IEEE*,

Abstract—This paper proposes a foreground-background separation (FBS) method with a novel foreground model based on convolutional sparse representation (CSR). In order to analyze the dynamic and static components of videos acquired under undesirable conditions, such as hardware, environmental, and power limitations, it is essential to establish an FBS method that can handle videos with low frame rates and various types of noise. Existing FBS methods have two limitations that prevent us from accurately separating foreground and background components from such degraded videos. First, they only capture either data-specific or general features of the components. Second, they do not include explicit models for various types of noise to remove them in the FBS process. To this end, we propose a robust FBS method with a CSR-based foreground model. This model can adaptively capture specific spatial structures scattered in imaging data. Then, we formulate FBS as a constrained multiconvex optimization problem that incorporates CSR, functions that capture general features, and explicit noise characterization functions for multiple types of noise. Thanks to these functions, our method captures both data-specific and general features to accurately separate the components from various types of noise even under low frame rates. To obtain a solution of the optimization problem, we develop an algorithm that alternately solves its two convex subproblems by newly established algorithms. Experiments demonstrate the superiority of our method over existing methods using two types of degraded videos: infrared and microscope videos.

Index Terms—Foreground-background separation, convolutional sparse representation (CSR), foreground modeling, alternating minimization

I. INTRODUCTION

FOREGROUND-BACKGROUND separation (FBS) is a preprocessing technique for decomposing video data into dynamic foreground and static background components [1], [2]. Since these components are crucial for subsequent processing, such as motion detection [3], moving object detection [4], small target detection [5], [6], background subtraction [7], [8], and cell segmentation [9], FBS is widely applied to the various types of videos, such as natural videos,

infrared (IR) videos, and microscope (MS) videos. However, some video data often suffer from several types of high-level noise [10], [11], such as Gaussian-like random noise, outliers, missing values, and stripe noise. In addition, they may suffer from low frame rates due to hardware limitations and power consumption. These severe degradations have a deleterious impact on the FBS performance. Therefore, the development of an FBS method that handles such *severely-degraded* videos can help resolve issues in related fields such as remote sensing, astronomical imaging, and biomedical/biological imaging [12], [13].

Existing FBS methods are broadly classified into a neural network-based approach [14]–[19] and an optimization-based approach [20]–[32]. The first approach constructs a neural network model that decomposes target videos into foreground and background components, capturing intricate features that are difficult to model manually. Methods taking the approach accurately separate featureful components from high-quality videos, but do not from severely-degraded videos because they do not incorporate appropriate characterizations for the various types of noise. In addition, because of the lack of clarity regarding criteria that FBS networks use to estimate these components, they might produce unexplainable results, especially when handling severely-degraded videos. Such lack of explainability can be fatal in the aforementioned fields, which often require clarity in the entire process of extracting meaningful data from observed videos, interpreting the information, and making decisions.

On the other hand, an optimization-based approach formulates FBS as an optimization problem that incorporates regularization functions that model the nature of foreground and background components and functions that characterize the noise. By leveraging these functions, this approach effectively separates noise from the components, enabling the development of robust FBS methods. Unlike a neural network-based approach, an optimization-based approach does not require training data, which makes it particularly suitable for severely-degraded videos. In terms of foreground modeling functions, there are two main categories: a sparsity model [20]–[25] and a smoothness and continuity model [26]–[32].

The well-known FBS method adopting the first model is robust principal component analysis [20], which inspired subsequent methods [21]–[25]. Although these methods are capable of capturing the sparsity of foreground components, they are unable to accurately estimate foreground components from videos contaminated with high-level noise or sparse noise

Manuscript received XXX, XXX; revised XXX XXX, XXX.

K. Naganuma is with the Institute of Engineering of Tokyo University of Agriculture and Technology, Tokyo, 184-8588, Japan (e-mail: k-naganuma@go.tuat.ac.jp).

S. Ono is with the Department of Computer Science, Institute of Science Tokyo, Yokohama, 226-8503, Japan (e-mail: ono@c.titech.ac.jp).

This work was supported in part by JST ACT-X Grant Number JPM-JAX23CJ, JST PRESTO under Grant JPMJPR21C4, and JST AdCORP under Grant JPMJKB2307, in part by JSPS KAKENHI under Grant 22H03610, 22H00512, 23H01415, 23K17461, 24K03119, and 24K22291, and in part by Grant-in-Aid for JSPS Fellows under Grant 25KJ0117.

because these types of noise have sparsely distributed high-intensity values. The second model characterizes foreground objects as spatial piecewise smoothness and slow motion based on their spatial correlation and temporal continuity, respectively [26]–[32]. However, this model may fail to separate the foreground component from low frame-rate videos that contain fast-moving objects. In addition, the two models are limited in their ability to recover the intricate detail structures of foreground objects specific to each video because they only capture features that appear in many videos.

To recover the intricate structures of a foreground component while removing various types of noise, FBS methods need to take an optimization approach equipped with mechanisms that capture data-specific features. One promising approach to build such an FBS method is by incorporating convolutional sparse representation (CSR) [33]–[37]. CSR models a component as the sum of convolutions between a basis (called a dictionary) and sparse coefficients, and thus efficiently captures specific spatial structures scattered in imaging data.¹ Due to its simple representation, CSR can learn a dictionary for data-specific features even from a single severely-degraded video, while guaranteeing interpretability in the FBS process. Here, a natural question arises: *By adopting CSC and regularization functions to capture data-specific and general features simultaneously, can we establish an FBS method that appropriately separates foreground and background components from severely-degraded videos?* To answer the question, we need to overcome the following technical difficulties.

- To capture both general features and data-specific features, CSR techniques need to be innovated in ranging from the design of an optimization problem to the development of an optimization algorithm.
- Optimization problems are typically designed by incorporating terms (e.g., CSR, noise characterizations, and video regularization functions). However, this increases the number of parameters that need to be adjusted manually and carefully.
- Although CSR has simpler structure than neural networks, optimization problems involving CSR are still nonconvex. Consequently, this presents a considerable challenge in developing an optimization algorithm that obtains a solution with meaningful background and foreground components and a basis of CSR.

Based on the above discussion, we propose a robust FBS with CSR-based foreground modeling (CSRFM). The main contributions are as follows.

- We introduce CSR into FBS as foreground modeling. Since foreground objects are scattered in several frames, CSR can adaptively capture their shapes and edges. Therefore, CSRFM thus accurately separates them even under highly noisy and low frame rate cases.
- We formulate FBS as a constrained multiconvex optimization problem incorporating the CSR-based model-

ing function. Our optimization problem is designed to separate foreground and background components while removing Gaussian, sparse, and stripe noise. In addition, instead of adding terms characterizing these types of noise to the objective function, they are imposed as hard constraints. This transforms complicated interdependent hyperparameters into independent parameters that can be set based on statistical information for noise.

- We develop an algorithm for solving optimization problems based on an alternating minimization (ALM). ALM requires solving convex subproblems with certain variables fixed. In our case, solvers for two convex subproblems are established based on the preconditioned primal-dual splitting algorithm (P-PDS) [44], [45] and the fast iterative shrinkage-thresholding algorithm (FISTA) [46]. P-PDS can automatically adjust the appropriate stepsizes based on the problem structure that changes with each iteration. In addition, FISTA also obtains a solution of the subproblem at a fast convergence rate without stepsize adjustment. These two algorithms allow us to solve each subproblem efficiently.

Experiments using IR videos and MS videos demonstrate the superiority of CSRFM to existing methods.

This paper is organized as follows. Section II gives preliminaries on CSR and ALM. In Section III, we present CSRFM. Experimental results and discussion are given in Section IV. Finally, we conclude the paper in Section V.

The preliminary version of this work, without the generalization of our method, comprehensive experimental comparison, or deeper discussion, has appeared in conference proceedings [47].

II. PRELIMINARIES

A. Notation

In this paper, we denote the sets of real numbers as \mathbb{R} . Vectors and matrices are denoted by lowercase bold letters (e.g., \mathbf{x}) and uppercase bold letters (e.g., \mathbf{X}), respectively. The i -th element of a vector \mathbf{x} is denoted by x_i or $[\mathbf{x}]_i$. Similarly, the element at the i -th row and j -th column of a matrix \mathbf{X} is denoted by $X_{i,j}$ or $[\mathbf{X}]_{i,j}$. The ℓ_1 , ℓ_2 , and operator norms are defined as $\|\mathbf{x}\|_1 := \sum_i |\mathbf{x}_i|$, $\|\mathbf{x}\|_2 := \sqrt{\sum_i \mathbf{x}_i^2}$, and $\|\mathcal{L}\|_{\text{op}} := \sup_{\mathbf{x} \neq \mathbf{0}} \|\mathcal{L}(\mathbf{x})\|_2 / \|\mathbf{x}\|_2$, respectively. We denote the ℓ_p ball centered by \mathbf{c} with a radius α as $B_{p,\alpha}^{\mathbf{c}} := \{\mathbf{y} \mid \|\mathbf{y} - \mathbf{c}\|_p \leq \alpha\}$. The adjoint operator of a linear operator \mathcal{L} is denoted as \mathcal{L}^* .

B. Convolutional Sparse Representation (CSR)

CSR models a signal \mathbf{x} as the sum of convolutions between a dictionary basis $\mathbf{d} := \{\mathbf{d}_1, \dots, \mathbf{d}_D\}$ and a sparse coefficient $\mathbf{a} := \{\mathbf{a}_1, \dots, \mathbf{a}_D\}$ [33]–[37]:

$$\min_{\mathbf{d}, \mathbf{a}} \frac{1}{2} \left\| \mathbf{x} - \sum_{d=1}^D \mathbf{d}_d * \mathbf{a}_d \right\|_2^2 + \lambda \sum_{d=1}^D \|\mathbf{a}_d\|_1 \text{ s.t. } \begin{cases} \mathbf{d}_1 \in B_{2,1}^0, \\ \vdots, \\ \mathbf{d}_D \in B_{2,1}^0, \end{cases} \quad (1)$$

where $*$ denotes the convolution operator. The first term guarantees the fidelity between the signal \mathbf{x} and the sum of

¹In the context of FBS, to capture the static nature of a background component for noiseless videos, some methods introduced SR [38]–[41], which represents a dictionary as a matrix [42], [43].

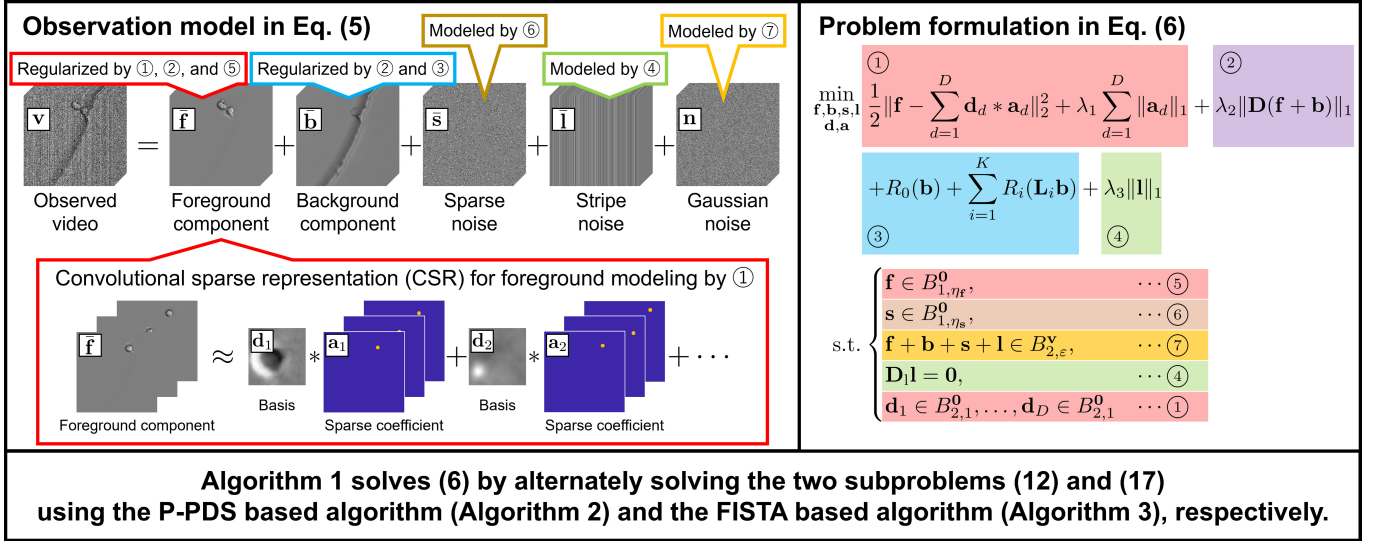


Fig. 1. Illustration of the proposed method, i.e., CSRFM.

convolutions between \mathbf{d} and \mathbf{a} . The second term promotes the sparsity of the coefficient \mathbf{a} . By combining these terms using the appropriate balancing parameter $\lambda > 0$, CSR can capture specific spatial structure scattered throughout the signal \mathbf{x} . The unit ℓ_2 ball constraints prevent the basis \mathbf{d} from absorbing all of the energy of the target signal \mathbf{x} .

C. Alternating Minimization for Multiconvex Optimization

This section introduces alternating minimization, which solves multiconvex optimization problems. We consider a multiconvex optimization problem of the following form:

$$\min_{\mathbf{x}_1, \dots, \mathbf{x}_n} f(\mathbf{x}_1, \dots, \mathbf{x}_n) + \sum_{i=1}^n g_i(\mathbf{x}_i), \quad (2)$$

where $f: \mathbb{R}^{N_1} \times \dots \times \mathbb{R}^{N_n} \rightarrow \mathbb{R}$ is a differentiable and *block multiconvex* function² and $g_i: \mathbb{R}^{N_i} \rightarrow (-\infty, \infty]$ ($\forall i = 1, \dots, n$) are proper lower-semicontinuous convex functions.

Under some conditions, the following procedures generate a sequence that converges to an optimal solution in a certain region close to an initial point [48]:

$$\begin{cases} \mathbf{x}_1^{(t+1)} \leftarrow \underset{\mathbf{x}_1}{\operatorname{argmin}} f_1^{(t)}(\mathbf{x}_1) + g_1(\mathbf{x}_1^{(t)}), \\ \vdots \\ \mathbf{x}_n^{(t+1)} \leftarrow \underset{\mathbf{x}_n}{\operatorname{argmin}} f_n^{(t)}(\mathbf{x}_n) + g_n(\mathbf{x}_n^{(t)}), \end{cases} \quad (3)$$

where for any $i = 1, \dots, n$

$$f_i^{(t)}(\mathbf{x}_i) = f(\mathbf{x}_1^{(t+1)}, \dots, \mathbf{x}_{i-1}^{(t+1)}, \mathbf{x}_i, \mathbf{x}_{i+1}^{(t)}, \dots, \mathbf{x}_n^{(t)}). \quad (4)$$

III. PROPOSED METHOD

Figure 1 shows a general diagram of the proposed method, CSRFM. In the following, we first introduce an observation model with three types of noise. Based on the model, we then

formulate the FBS problem as a constrained multiconvex optimization problem involving CSR-based foreground modeling. Finally, we describe an ALM-based algorithm to solve the optimization problem.

A. Problem Formulation

Let $\mathbf{V}_1, \dots, \mathbf{V}_{n_3} \in \mathbb{R}^{n_1 \times n_2}$ be n_3 observed frames. We handle the observed frames in a vectorized form as $\mathbf{v} = [\operatorname{vec}(\mathbf{V}_1)^T \dots \operatorname{vec}(\mathbf{V}_{n_3})^T]^T \in \mathbb{R}^{n_1 n_2 n_3}$, where $\operatorname{vec}: \mathbb{R}^{n_1 \times n_2} \rightarrow \mathbb{R}^{n_1 n_2}$ represents the vectorization operator. Then, consider that the observed video is modeled by

$$\mathbf{v} = \bar{\mathbf{f}} + \bar{\mathbf{b}} + \bar{\mathbf{s}} + \bar{\mathbf{l}} + \mathbf{n}, \quad (5)$$

where $\bar{\mathbf{f}}$, $\bar{\mathbf{b}}$, $\bar{\mathbf{s}}$, $\bar{\mathbf{l}}$, and \mathbf{n} are the true foreground component, the true background component, sparsely distributed noise (e.g., missing values and outliers), stripe noise, and random noise, respectively.

Based on the model in (5), we newly formulate FBS as a multiconvex optimization problem of the following form:

$$\begin{aligned} \min_{\mathbf{f}, \mathbf{b}, \mathbf{s}, \mathbf{l}} \frac{1}{2} \left\| \mathbf{f} - \sum_{d=1}^D \mathbf{d}_d \ast \mathbf{a}_d \right\|_2^2 + \lambda_1 \sum_{d=1}^D \|\mathbf{a}_d\|_1 + \lambda_2 \|\mathbf{D}(\mathbf{f} + \mathbf{b})\|_1 \\ + R_0(\mathbf{b}) + \sum_{i=1}^K R_i(\mathbf{L}_i \mathbf{b}) + \|\mathbf{l}\|_1 \end{aligned}$$

$$\text{s.t. } \begin{cases} \mathbf{f} \in B_{1, \eta_f}^0, \\ \mathbf{s} \in B_{1, \eta_s}^0, \\ \mathbf{f} + \mathbf{b} + \mathbf{s} + \mathbf{l} \in B_{2, \varepsilon}^y, \\ \mathbf{D}\mathbf{l} = \mathbf{0}, \\ \mathbf{d}_1 \in B_{2,1}^0, \dots, \mathbf{d}_D \in B_{2,1}^0. \end{cases} \quad (6)$$

These terms and constraints have the following roles.

1) *CSR for f*: The first and second terms (with a balancing parameter $\lambda_1 > 0$) and the constraints in fifth row build CSR, which captures similar structures over frames by simultaneously estimating a basis $\mathbf{d}_1, \dots, \mathbf{d}_D$ (representing the

²A function $f(\mathbf{x}_1, \dots, \mathbf{x}_n)$ is called *block multiconvex* if, for each i , f is a convex function of \mathbf{x}_i while all the other blocks are fixed.

Algorithm 1 Solver for the main FBS problem (6)

Input: $\mathbf{f}^{(0)}, \mathbf{b}^{(0)}, \mathbf{s}^{(0)}, \mathbf{l}^{(0)}, \mathbf{a}^{(0)}, \mathbf{d}^{(0)}$
Output: $\mathbf{f}^{(t)}, \mathbf{b}^{(t)}, \mathbf{d}^{(t)}$

- 1: Initialize $t = 0, \mathbf{f}^{(0)}, \mathbf{b}^{(0)}, \mathbf{s}^{(0)}, \mathbf{l}^{(0)}, \mathbf{a}^{(0)}, \mathbf{d}^{(0)}$;
- 2: **while** A stopping criterion are not satisfied **do**
- 3: $\mathbf{f}^{(t+1)}, \mathbf{b}^{(t+1)}, \mathbf{s}^{(t+1)}, \mathbf{l}^{(t+1)}, \mathbf{a}^{(t+1)}$
 $\leftarrow \underset{\mathbf{f}, \mathbf{b}, \mathbf{s}, \mathbf{l}, \mathbf{a}}{\operatorname{argmin}} f_1^{(t)}(\mathbf{f}, \mathbf{b}, \mathbf{s}, \mathbf{l}, \mathbf{a}) + g_1(\mathbf{f}, \mathbf{b}, \mathbf{s}, \mathbf{l}, \mathbf{a})$
 i.e., solving Prob. (12) by Algorithm 2;
- 4: $\mathbf{d}^{(t+1)} \leftarrow \underset{\mathbf{d}}{\operatorname{argmin}} f_2^{(t)}(\mathbf{d}) + g_2(\mathbf{d})$
 i.e., solving Prob. (17) by Algorithm 3;
- 5: $t \leftarrow t + 1$;

edges or shapes of foreground objects) and their corresponding sparse coefficients $\mathbf{a}_1, \dots, \mathbf{a}_D$ (representing the locations). By referring to the sum of the convolutions of $\mathbf{d}_1, \dots, \mathbf{d}_D$ and $\mathbf{a}_1, \dots, \mathbf{a}_D$ estimated simultaneously with \mathbf{f} , CSRFM can recover the structures of \mathbf{f} more accurately.

2) *A Sparsity Constraint for \mathbf{f} :* The first constraint guarantees the sparsity of the foreground component \mathbf{f} with the ℓ_1 ball with a radius η_f . By varying η_f , we can control the sparsity of \mathbf{f} . Using this constraint instead of a sparse term avoids adjusting the hyperparameter in response to changes of background modeling functions or noise conditions.

3) *Background Modeling:* The sum of the fourth and fifth terms is a general form of background modeling including linear operators $\mathbf{L}_1, \dots, \mathbf{L}_K$ and proper lower-semicontinuous convex functions R_0, \dots, R_K . Some examples of applying specific background modeling to the general form will be shown in Section III-C.

4) *Total Variation Regularization for \mathbf{f} and \mathbf{b} :* The third term promotes the spatial piecewise smoothness of \mathbf{f} and \mathbf{b} by the total variation regularization with a balancing parameter $\lambda_2 > 0$. The total variation regularization incorporates a spatial difference operator $\mathbf{D} := [\mathbf{D}_v^\top \mathbf{D}_h^\top]^\top \in \mathbb{R}^{2n_1 n_2 n_3 \times n_1 n_2 n_3}$, where \mathbf{D}_v and \mathbf{D}_h are the vertical and horizontal difference operators with the Neumann boundary condition: let $[\operatorname{vec}(\mathbf{Y}_1)^\top \dots \operatorname{vec}(\mathbf{Y}_{n_3})^\top]^\top = \mathbf{D}_v \mathbf{x}$ and $[\operatorname{vec}(\mathbf{W}_1)^\top \dots \operatorname{vec}(\mathbf{W}_{n_3})^\top]^\top = \mathbf{D}_h \mathbf{x}$ for a time series component $\mathbf{x} = [\operatorname{vec}(\mathbf{X}_1)^\top \dots \operatorname{vec}(\mathbf{X}_{n_3})^\top]^\top$, then for any $k = 1, \dots, n_3$

$$[\mathbf{Y}_k]_{i,j} = \begin{cases} [\mathbf{X}_k]_{i+1,j} - [\mathbf{X}_k]_{i,j}, & \text{if } i < n_1; \\ 0, & \text{otherwise,} \end{cases} \quad (7)$$

$$[\mathbf{W}_k]_{i,j} = \begin{cases} [\mathbf{X}_k]_{i,j+1} - [\mathbf{X}_k]_{i,j}, & \text{if } j < n_2; \\ 0, & \text{otherwise.} \end{cases} \quad (8)$$

5) *Handling Three Types of Noise:* The second constraints guarantee the sparsity of \mathbf{s} . The third constraint guarantees the data-fidelity to an observed video \mathbf{v} . Using these constraints instead of data-fidelity and sparse terms allows us to easily adjust the hyperparameters, since the parameters ε and η_s can be determined based only on the statistical information of these types of noise, rather than relative weights to the terms of the objective function. Indeed, this kind of constrained

Algorithm 2 P-PDS solver for the subproblem (12)

Input: $\mathbf{f}^{(t)}, \mathbf{b}^{(t)}, \mathbf{s}^{(t)}, \mathbf{l}^{(t)}, \mathbf{a}^{(t)}, \tilde{\mathbf{d}} = \mathbf{d}^{(t)}$
Output: $\mathbf{f}^{(l)}, \mathbf{b}^{(l)}, \mathbf{s}^{(l)}, \mathbf{l}^{(l)}, \mathbf{a}^{(l)}$

- 1: Initialize $l = 0, \mathbf{z}_{1,1}, \dots, \mathbf{z}_{1,K}, \mathbf{z}_2, \mathbf{z}_3$;
- 2: Set $\mathbf{f}^{(l)}, \mathbf{b}^{(l)}, \mathbf{s}^{(l)}, \mathbf{l}^{(l)}, \mathbf{a}^{(l)} \leftarrow \mathbf{f}^{(t)}, \mathbf{b}^{(t)}, \mathbf{s}^{(t)}, \mathbf{l}^{(t)}, \mathbf{a}^{(t)}$;
- 3: Set stepsizes $\gamma_f, \gamma_b, \gamma_s, \gamma_a, \gamma_z$ as (13);
- 4: **while** A stopping criterion is not satisfied **do**
- 5: $\mathbf{f}' \leftarrow \mathbf{f}^{(l)} - \gamma_f(\mathbf{z}_2^{(l)} + \mathbf{D}^\top \mathbf{z}_3^{(l)} + \mathbf{z}_4^{(l)})$;
- 6: $\mathbf{f}^{(l+1)} \leftarrow \operatorname{prox}_{\gamma_f \ell_{B_0^{f, \eta_f}}}(\mathbf{f}')$ by the algorithm in [49];
- 7: $\mathbf{b}' \leftarrow \mathbf{b}^{(l)} - \gamma_b(\sum_{i=1}^K \mathbf{L}_i^\top \mathbf{z}_{1,K}^{(l)} + \mathbf{D}^\top \mathbf{z}_3^{(l)} + \mathbf{z}_4^{(l)})$;
- 8: $\mathbf{b}^{(l+1)} \leftarrow \operatorname{prox}_{\gamma_b R_0}(\mathbf{b}')$;
- 9: $\mathbf{s}' \leftarrow \mathbf{s}^{(l)} - \gamma_s \mathbf{z}_4^{(l)}$;
- 10: $\mathbf{s}^{(l+1)} \leftarrow \operatorname{prox}_{\gamma_s \ell_{B_0^{s, \eta_s}}}(\mathbf{s}')$ by the algorithm in [49];
- 11: $\mathbf{l}^{(l+1)} \leftarrow \operatorname{prox}_{\|\cdot\|_1}(\mathbf{l}^{(l)} - \gamma_l(\mathbf{z}_4^{(l)} + \mathbf{D}_1^\top \mathbf{z}_5^{(l)}))$;
- 12: **for** $d = 1, \dots, D$ **do**
- 13: $\mathbf{a}'_d \leftarrow \mathbf{a}_d^{(l)} - \gamma_{a_d}(\mathbf{c}_{\mathbf{a}_d}^* (-\mathbf{z}_2^{(l)}))$;
- 14: $\mathbf{a}_d^{(l+1)} \leftarrow \operatorname{prox}_{\gamma_{a_d} \lambda_1 \|\cdot\|_1}(\mathbf{a}'_d)$;
- 15: $\tilde{\mathbf{b}} \leftarrow 2\mathbf{b}^{(l+1)} - \mathbf{b}^{(l)}$;
- 16: $\tilde{\mathbf{f}} \leftarrow 2\mathbf{f}^{(l+1)} - \mathbf{f}^{(l)}$;
- 17: $\tilde{\mathbf{s}} \leftarrow 2\mathbf{s}^{(l+1)} - \mathbf{s}^{(l)}$;
- 18: $\tilde{\mathbf{l}} \leftarrow 2\mathbf{l}^{(l+1)} - \mathbf{l}^{(l)}$;
- 19: $\tilde{\mathbf{a}} \leftarrow \sum_{d=1}^D \mathbf{c}_{\mathbf{a}_d} (2\mathbf{a}_d^{(l+1)} - \mathbf{a}_d^{(l)})$;
- 20: **for** $i = 1, \dots, K$ **do**
- 21: $\mathbf{z}'_{1,i} \leftarrow \mathbf{z}_{1,i}^{(l)} + \gamma_z \mathbf{L}_i \tilde{\mathbf{b}}$;
- 22: $\mathbf{z}_{1,i}^{(l+1)} \leftarrow \mathbf{z}'_{1,i} - \gamma_z \operatorname{prox}_{\frac{1}{\gamma_z} R_i}(\frac{1}{\gamma_z} \mathbf{z}'_{1,i})$;
- 23: $\mathbf{z}'_2 \leftarrow \mathbf{z}_2^{(l)} + \gamma_z(\tilde{\mathbf{f}} - \tilde{\mathbf{a}})$;
- 24: $\mathbf{z}_2^{(l+1)} \leftarrow \mathbf{z}'_2 - \gamma_z \operatorname{prox}_{\frac{1}{2\gamma_z} \|\cdot\|_2^2}(\frac{1}{\gamma_z} \mathbf{z}'_2)$;
- 25: $\mathbf{z}'_3 \leftarrow \mathbf{z}_3^{(l)} + \gamma_z \mathbf{D}(\tilde{\mathbf{b}} + \tilde{\mathbf{f}})$;
- 26: $\mathbf{z}_3^{(l+1)} \leftarrow \mathbf{z}'_3 - \gamma_z \operatorname{prox}_{\frac{\lambda_1}{\gamma_z} \|\cdot\|_1}(\frac{1}{\gamma_z} \mathbf{z}'_3)$;
- 27: $\mathbf{z}'_4 \leftarrow \mathbf{z}_4^{(l)} + \gamma_z(\tilde{\mathbf{b}} + \tilde{\mathbf{f}} + \tilde{\mathbf{s}} + \tilde{\mathbf{l}})$;
- 28: $\mathbf{z}_4^{(l+1)} \leftarrow \mathbf{z}'_4 - \gamma_z \operatorname{prox}_{\frac{1}{\gamma_z} \ell_{B_{2,\varepsilon}^{\mathbf{y}}}}}(\frac{1}{\gamma_z} \mathbf{z}'_4)$;
- 29: $\mathbf{z}_5^{(l+1)} \leftarrow \mathbf{z}_5^{(l)} + \gamma_z \mathbf{D}_1 \tilde{\mathbf{l}}$;
- 30: $l \leftarrow l + 1$;

formulation has played an important role in facilitating the parameter setting of signal recovery problems [50]–[54].

The sixth term controls the intensity of a stripe noise component \mathbf{l} . The fourth constraint is the flatness constraint [55], which captures the vertical flatness and temporal invariance by imposing zero to all the values of the vertical and temporal gradients of \mathbf{l} using a difference operator $\mathbf{D}_1 = [\mathbf{D}_v^\top \mathbf{D}_t^\top]^\top \in \mathbb{R}^{2n_1 n_2 n_3 \times n_1 n_2 n_3}$.³ Here, \mathbf{D}_v is the vertical difference operator defined in Eq. (7) and \mathbf{D}_t is the temporal difference operator with the Neumann boundary condition: let $[\operatorname{vec}(\mathbf{Y}_1)^\top \dots \operatorname{vec}(\mathbf{Y}_{n_3})^\top]^\top = \mathbf{D}_t \mathbf{x}$, then for any $k = 1, \dots, n_3$

$$[\mathbf{Y}_k]_{i,j} = \begin{cases} [\mathbf{X}_{k+1}]_{i,j} - [\mathbf{X}_k]_{i,j}, & \text{if } k < n_3; \\ 0, & \text{otherwise.} \end{cases} \quad (9)$$

³For data with horizontally featured stripe noise, we rotate the data 90 degrees in the spatial direction before optimization.

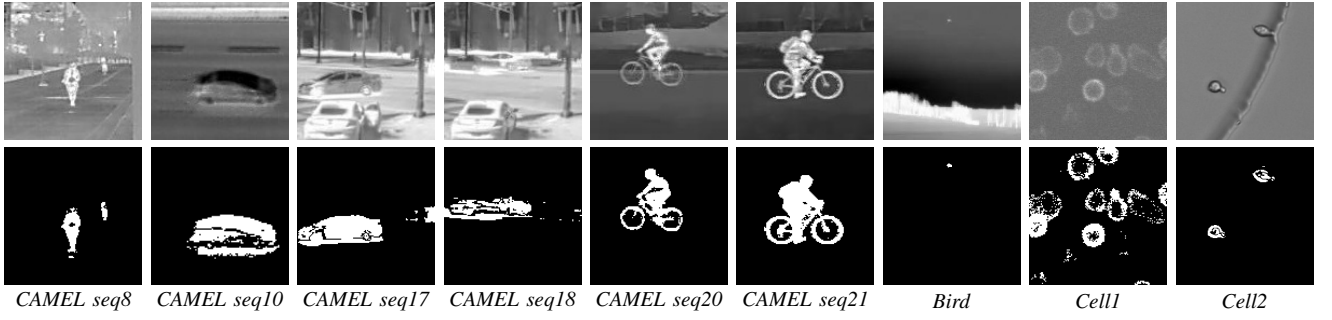


Fig. 2. The top row shows the ground-truth video frames. The bottom row shows the pseudo ground-truth foreground maps. *CAMEL seq8*, *CAMEL seq10*, *CAMEL seq17*, *CAMEL seq18*, *CAMEL seq20*, *CAMEL seq21*, and *Bird* are IR videos. *Cell1* and *Cell2* are MS videos.

Algorithm 3 FISTA solver for the subproblem (17)

Input: $\mathbf{d}^{(t)}, \tilde{\mathbf{f}} = \mathbf{f}^{(t+1)}, \tilde{\mathbf{a}} = \mathbf{a}^{(t+1)}, \gamma$

Output: $\mathbf{d}^{(l)}$

- 1: Initialize $l = 0, \tau^{(0)} = 1, \mathbf{z}_1, \dots, \mathbf{z}_D$;
 - 2: **while** A stopping criterion is not satisfied **do**
 - 3: $\tau^{(l+1)} \leftarrow \frac{1 + \sqrt{1 + 4\tau^{(l)}\tau^{(l)}}}{2}$;
 - 4: **for** $d = 1, \dots, D$ **do**
 - 5: $\mathbf{d}'_d \leftarrow \mathbf{z}_d^{(l)} - \gamma \mathfrak{A}_{\tilde{\mathbf{a}}_d}^* (\sum_{d=1}^D \mathfrak{A}_{\tilde{\mathbf{a}}_d}(\mathbf{d}_d^{(l)}) - \tilde{\mathbf{f}})$;
 - 6: $\mathbf{d}_d^{(l)} \leftarrow \text{prox}_{\gamma \iota_{B_{2,1}^0}}(\mathbf{d}'_d)$;
 - 7: $\mathbf{z}_d^{(l+1)} \leftarrow \mathbf{d}_d^{(l+1)} + \frac{\tau^{(l)} - 1}{\tau^{(l+1)}} (\mathbf{d}_d^{(l+1)} - \mathbf{d}_d^{(l)})$;
 - 8: $l \leftarrow l + 1$;
-

Actually, this flatness constraint plays an important role to accurately characterize the stripe noise in the context of remote sensing data analysis [56]–[58]. If stripe noise changes over time, the difference operator \mathbf{D}_1 is designed as $\mathbf{D}_1 = \mathbf{D}_v \in \mathbb{R}^{n_1 n_2 n_3 \times n_1 n_2 n_3}$.

B. Optimization

Using indicator functions⁴ $\iota_{B_{2,\varepsilon}^y}, \iota_{B_{1,\eta_f}^0}$, and ι_{B_{1,η_s}^0} of norm balls $B_{2,\varepsilon}^y$, B_{1,η_s}^0 , and B_{1,η_f}^0 , we reformulate Prob. (6) into the following equivalent optimization problem:

$$\begin{aligned} \min_{\mathbf{f}, \mathbf{b}, \mathbf{s}, \mathbf{l}, \mathbf{a}, \mathbf{d}} \quad & \frac{1}{2} \left\| \mathbf{f} - \sum_{d=1}^D \mathbf{d}_d * \mathbf{a}_d \right\|_2^2 + \lambda_1 \sum_{d=1}^D \|\mathbf{a}_d\|_1 + \lambda_2 \|\mathbf{D}(\mathbf{f} + \mathbf{b})\|_1 \\ & + R_0(\mathbf{b}) + \sum_{i=1}^K R_i(\mathbf{L}_i \mathbf{b}) + \|\mathbf{l}\|_1 + \iota_{B_{1,\eta_f}^0}(\mathbf{f}) + \iota_{B_{1,\eta_s}^0}(\mathbf{s}) \\ & + \iota_{B_{2,\varepsilon}^y}(\mathbf{f} + \mathbf{b} + \mathbf{s} + \mathbf{l}) + \iota_{\{0\}}(\mathbf{D}_1 \mathbf{l}) + \sum_{d=1}^D \iota_{B_{2,1}^0}(\mathbf{d}_d). \end{aligned} \quad (10)$$

Since the first term is a multiconvex function and the other terms are convex functions, Prob. (6) can be seen as a specific form of Prob. (2). To solve this type of optimization problems, one often updates the variables one by one. However, since each the update process strongly depends on the current states of the other variables, this approach can produce a sequence that converges to a local minimum that includes meaningless

⁴For a given nonempty closed set C , the indicator function of C is defined as $\iota_C(\mathcal{X}) := 0$, if $\mathcal{X} \in C$; ∞ , otherwise.

components. Therefore, we take an approach to update some variables simultaneously. Specifically, we set

$$\begin{aligned} f(\mathbf{f}, \mathbf{b}, \mathbf{s}, \mathbf{l}, \mathbf{a}, \mathbf{d}) &= \frac{1}{2} \left\| \mathbf{f} - \sum_{d=1}^D \mathbf{d}_d * \mathbf{a}_d \right\|_2^2, \\ g_1(\mathbf{f}, \mathbf{b}, \mathbf{s}, \mathbf{l}, \mathbf{a}) &= \lambda_1 \sum_{d=1}^D \|\mathbf{a}_d\|_1 + \lambda_2 \|\mathbf{D}(\mathbf{f} + \mathbf{b})\|_1 + R_0(\mathbf{b}) \\ &+ \sum_{i=0}^K R_i(\mathbf{L}_i \mathbf{b}) + \|\mathbf{l}\|_1 + \iota_{B_{1,\eta_f}^0}(\mathbf{f}) \\ &+ \iota_{B_{1,\eta_s}^0}(\mathbf{s}) + \iota_{B_{2,\varepsilon}^y}(\mathbf{f} + \mathbf{b} + \mathbf{s} + \mathbf{l}) \\ &+ \iota_{\{0\}}(\mathbf{D}_1 \mathbf{l}), \\ g_2(\mathbf{d}) &= \sum_{d=1}^D \iota_{B_{2,1}^0}(\mathbf{d}_d), \end{aligned} \quad (11)$$

and alternately solving two subproblems for $f_1^t + g_1$ and $f_2^t + g_2$ to update the variables $\mathbf{f}, \mathbf{b}, \mathbf{s}, \mathbf{l}, \mathbf{a}$ and the variable \mathbf{d} .

Algorithm 1 shows an ALM-based algorithm to solve Prob. (1).⁵ Here, we describe the details of algorithms solving each subproblem.

1) *Updating $\mathbf{f}, \mathbf{b}, \mathbf{s}, \mathbf{l}$, and \mathbf{a}* : With $\mathbf{d}^{(t)}$ fixed, the first subproblem of Prob. (10) with respect to $\mathbf{f}, \mathbf{b}, \mathbf{s}, \mathbf{l}$, and \mathbf{a} is written as the following optimization problem:

$$\begin{aligned} \min_{\mathbf{f}, \mathbf{b}, \mathbf{s}, \mathbf{l}, \mathbf{a}} \quad & \iota_{B_{1,\eta_f}^0}(\mathbf{f}) + R_0(\mathbf{b}) + \iota_{B_{1,\eta_s}^0}(\mathbf{s}) + \|\mathbf{l}\|_1 + \lambda_1 \sum_{d=1}^D \|\mathbf{a}_d\|_1 \\ & + \sum_{i=1}^K R_i(\mathbf{L}_i \mathbf{b}) + \frac{1}{2} \left\| \mathbf{f} - \sum_{d=1}^D \mathbf{d}_d^{(t)} * \mathbf{a}_d \right\|_2^2 \\ & + \lambda_2 \|\mathbf{D}(\mathbf{f} + \mathbf{b})\|_1 + \iota_{B_{2,\varepsilon}^y}(\mathbf{f} + \mathbf{b} + \mathbf{s} + \mathbf{l}) + \iota_{\{0\}}(\mathbf{D}_1 \mathbf{l}). \end{aligned} \quad (12)$$

Prob. (12) can be solved by P-PDS [44], [45].

We show the detailed algorithm in Algorithm 2. Following a method [45] that selects reasonable stepsize, the parameters $\gamma_f, \gamma_b, \gamma_s, \gamma_a$, and γ_z are determined as follows:

$$\begin{aligned} \gamma_f &= \frac{1}{10}, \gamma_b = \frac{1}{9 + \sum_{i=1}^K \|\mathbf{L}_i\|_{\text{op}}^2}, \gamma_s = 1, \gamma_l = \frac{1}{9}, \\ \gamma_a &= \frac{1}{\sum_{d=1}^D \|\mathbf{c}_{\mathbf{a}_d}\|_{\text{op}}^2}, \gamma_z = \frac{1}{4+D}, \end{aligned} \quad (13)$$

⁵It is difficult to confirm whether Algorithm 1 satisfies the theoretical convergence condition described in [48]. However, we observed in experiments (see Section IV) that our algorithm generate stable results.

TABLE I
HYPERPARAMETER SETTINGS IN EACH METHOD.

Methods	Recommended parameters	Parameter search ranges
RPCA [20]	$\lambda = \frac{1}{\sqrt{\max(n_1, n_2)}}$	$\lambda = \frac{\kappa}{\sqrt{\max(n_1, n_2)}}, \kappa \in \{10^{-2}, 10^{-1}, 10^0, 10^1, 10^2\}$
GNNLSM [25]	$\tau = 300,$ $\gamma = 0.001$	$\tau = 300\kappa_1, \kappa_1 \in \{10^{-1}, 10^0, 10^1\},$ $\gamma = 0.001\kappa_2, \kappa_2 \in \{10^{-1}, 10^0, 10^1\}$
TVRPCA [28]	$\lambda_1 = \frac{0.4}{n_1 n_2},$ $\lambda_2 = \frac{2}{n_1 n_2},$ $\lambda_3 = \frac{0.1}{n_1 n_2}$	$\lambda_1 = \frac{0.4\kappa_1}{n_1 n_2}, \kappa_1 \in \{10^{-2}, 10^{-1}, 10^0, 10^1, 10^2\},$ $\lambda_2 = \frac{2\kappa_2}{n_1 n_2}, \kappa_2 \in \{10^{-2}, 10^{-1}, 10^0, 10^1, 10^2\},$ $\lambda_3 = \frac{0.1\kappa_3}{n_1 n_2}, \kappa_3 \in \{10^{-2}, 10^{-1}, 10^0, 10^1, 10^2\}$
PRPCA [29]	$\lambda_L \in \{1, 2, 4, 6, 8, 10\},$ $\lambda_S = \frac{0.01}{\sqrt{n_1 n_2}},$ $\lambda_E = \frac{0.001}{\sqrt{n_1 n_2}}$	$\lambda_L \in \{1, 2, 4, 6, 8, 10\},$ $\lambda_S = \frac{0.01\kappa_1}{\sqrt{n_1 n_2}}, \kappa_1 \in \{10^{-2}, 10^{-1}, 10^0, 10^1, 10^2\},$ $\lambda_E = \frac{0.001\kappa_2}{\sqrt{n_1 n_2}}, \kappa_2 \in \{10^{-2}, 10^{-1}, 10^0, 10^1, 10^2\}$
SRTC [31]	$\lambda = 0.5$	$\lambda = 0.5\kappa, \kappa \in \{10^{-2}, 10^{-1}, 10^0, 10^1, 10^2\}$
SS-RTD [32]	$\lambda \in \{0.2, 0.4, 0.6, 0.8, 1.0\}$	$\lambda \in \{0.2, 0.4, 0.6, 0.8, 1.0\}$
FactorDVP-T [19]	Learning Rate $\in \{10^{-4}, 10^{-3}, 10^{-2}\}$ $r \in \{1, 3\}$	Learning Rate $\in \{10^{-4}, 10^{-3}, 10^{-2}\}$ $r \in \{1, 3\}$
CSRFM (Ours)	–	$\lambda_2 \in \{10^{-2}, 10^{-1}, 10^0, 10^1, 10^2\},$ $\lambda_{LR} \in \{10^{-2}, 10^{-1}, 10^0, 10^1, 10^2\}$
CSRFM (Ours)	–	$\lambda_2 \in \{10^{-2}, 10^{-1}, 10^0, 10^1, 10^2\}$

TABLE II
PARAMETER SETTINGS RELATED TO CSR.

Datasets	η_f	D	The size of \mathbf{d}
<i>CAMEL seq8</i>	9000	2	25×25
<i>CAMEL seq10</i>	6000	6	25×25
<i>CAMEL seq17</i>	12000	12	51×51
<i>CAMEL seq18</i>	15000	12	51×51
<i>CAMEL seq20</i>	9000	3	41×41
<i>CAMEL seq21</i>	9000	2	41×41
<i>Bird</i>	2000	6	11×11
<i>Cell1</i>	7000	6	31×31
<i>Cell2</i>	7000	6	31×31

where $\mathfrak{C}_{\mathbf{d}_d^{(t)}}(\mathbf{a}) = \mathbf{d}_d^{(t)} * \mathbf{a}$. The proximity operators⁶ of $\|\cdot\|_1$, $\frac{1}{2}\|\cdot\|_2^2$, and $\iota_{B_{2,\varepsilon}^{\mathbf{y}}}$ (in lines 11, 16, and 18 of Algorithm 2) are respectively calculated as

$$[\text{prox}_{\alpha\|\cdot\|_1}(\mathbf{x})]_i = \text{sgn}(x_i) \max\{|x_i| - \alpha, 0\}, \quad (14)$$

$$\text{prox}_{\frac{\alpha}{2}\|\cdot\|_2^2}(\mathbf{x}) = \frac{\mathbf{x}}{1 + \alpha}, \quad (15)$$

$$\text{prox}_{\alpha\iota_{B_{2,\varepsilon}^{\mathbf{y}}}}(\mathbf{x}) = \begin{cases} \mathbf{x}, & \text{if } \mathbf{x} \in B_{2,\varepsilon}^{\mathbf{y}}; \\ \mathbf{v} + \frac{\varepsilon(\mathbf{x} - \mathbf{v})}{\|\mathbf{x} - \mathbf{v}\|_2}, & \text{otherwise.} \end{cases} \quad (16)$$

The proximity operator of $\iota_{B_{1,\eta}^{\mathbf{0}}}$ can be efficiently computed by the ℓ_1 ball projection algorithm [49].

2) *Updating d*: With \mathbf{f} , \mathbf{b} , \mathbf{s} , \mathbf{l} , and \mathbf{a} fixed, the subproblem of Prob. (6) with respect to \mathbf{d} is written as the following

⁶The proximity operator of a proper lower semicontinuous convex function f with a parameter $\alpha > 0$ is defined as $\text{prox}_{\alpha f}(\mathbf{x}) := \arg\min_{\mathbf{y}} f(\mathbf{y}) + \frac{1}{2\alpha}\|\mathbf{x} - \mathbf{y}\|_2^2$.

optimization problem:

$$\min_{\mathbf{d}} \frac{1}{2} \left\| \mathbf{f}^{(t+1)} - \sum_{d=1}^D \mathbf{d}_d * \mathbf{a}_d^{(t+1)} \right\|_2^2 + \sum_{d=1}^D \iota_{B_{2,1}^{\mathbf{0}}}(\mathbf{d}_d). \quad (17)$$

Prob. (17) is can be approximately solved by FISTA [46]. Algorithm 3 shows the detailed processes. The stepsize parameter γ is set as $\gamma = \frac{1}{\sum_{d=1}^D \|\mathfrak{A}_{\mathbf{a}_d}\|_{\text{op}}^2}$, where $\mathfrak{A}_{\mathbf{a}_d}(\mathbf{d}) = \mathbf{d} * \mathbf{a}_d$.

C. Examples of Applying Specific Background Modeling

We apply some specific functions into the background modeling functions in Prob. (6).

First, let us consider low-rank modeling, which often appears in numerous FBS methods. This modeling promotes the low rankness of a background component matrix $\mathbf{B} = [\mathbf{b}_1, \dots, \mathbf{b}_{n_3}] \in \mathbb{R}^{n_3 \times n_1 n_2}$ using the nuclear norm, defined as

$$\|\mathbf{B}\|_* := \sum_{i=1}^q s_i(\mathbf{B}), \quad (18)$$

where $s_i(\mathbf{B})$ is the i -th singular value of \mathbf{B} and $q = \min\{n_1 n_2, n_3\}$. Letting $K = 0$ and $R_0 = \lambda_{LR}\|\cdot\|_*$, we can apply the low-rank modeling to Prob. (6). By using a vectorizing operator $\text{vec}(\mathbf{B}) = [\mathbf{b}_1^\top, \dots, \mathbf{b}_{n_3}^\top]^\top$ and a matrix-izing operator $\text{mat}(\mathbf{b}) = [\mathbf{b}_1, \dots, \mathbf{b}_{n_3}]$, the steps 7 and 8 in Algorithm 2 become

$$\mathbf{b}' \leftarrow \mathbf{b}^{(l)} - \gamma_{\mathbf{b}}(\mathbf{D}^\top \mathbf{z}_3^{(l)} + \mathbf{z}_4^{(l)}), \quad (19)$$

$$\mathbf{b}^{(l+1)} \leftarrow \text{vec}(\text{prox}_{\gamma_{\mathbf{b}}\lambda_{LR}\|\cdot\|_*}(\text{mat}(\mathbf{b}'))), \quad (20)$$

and the steps 20-22 are eliminated. Here, the proximity operator of $\|\cdot\|_*$ with a parameter $\gamma > 0$ can be calculated as

TABLE III
MPSNR, MSSIM, AND AUC VALUES OF THE FBS RESULTS IN CASE 1.

Video	Measure	Methods							
		RPCA [20]	GNNLSM [25]	TVRPCA [28]	PRPCA [29]	SRTC [31]	SS-RTD [32]	FactorDVP-T [19]	CSRFM (LR) CSRFM (SC)
CAMEL seq8	MPSNR f	19.95	24.18	19.51	19.23	30.79	32.16	25.38	<u>32.32</u> 32.68
	MPSNR b	30.31	18.60	27.52	28.35	<u>31.75</u>	31.57	26.05	30.78 34.87
	MSSIM f	0.0789	0.7638	0.0647	0.0606	0.4584	0.2961	0.1568	<u>0.6546</u> 0.6314
	MSSIM b	0.7938	0.2482	0.8176	0.7892	0.8493	0.7960	0.9273	0.9443 <u>0.9374</u>
	AUC	0.9040	0.5043	0.9207	0.5697	0.9703	0.9809	0.9799	<u>0.9867</u> 0.9921
CAMEL seq10	MPSNR f	20.04	27.17	19.60	19.16	30.68	27.70	17.92	31.17 <u>31.11</u>
	MPSNR b	30.56	18.59	28.06	30.26	32.00	30.27	17.97	36.32 <u>32.72</u>
	MSSIM f	0.1031	<u>0.5854</u>	0.0876	0.0472	0.5772	0.3062	0.1111	0.6211 0.5763
	MSSIM b	0.7502	0.2011	0.7828	0.7480	0.8176	0.7582	0.8635	<u>0.9408</u> 0.9549
	AUC	0.8067	0.5070	0.8062	0.5240	0.9441	0.9256	0.6300	0.9659 <u>0.9626</u>
CAMEL seq17	MPSNR f	19.87	24.97	19.27	19.20	29.22	28.76	19.75	<u>30.54</u> 31.45
	MPSNR b	28.90	18.55	26.15	30.61	33.01	31.66	20.16	30.76 <u>32.42</u>
	MSSIM f	0.0980	<u>0.6673</u>	0.0757	0.0553	0.7637	0.4141	0.0935	0.6018 0.5708
	MSSIM b	0.8381	0.3718	0.8588	0.8436	0.8864	0.8548	<u>0.9058</u>	0.9023 0.9350
	AUC	0.7610	0.5001	0.7607	0.5210	0.9415	0.9414	0.6865	<u>0.9612</u> 0.9711
CAMEL seq18	MPSNR f	19.86	22.94	19.24	18.66	<u>27.95</u>	28.05	22.52	<u>30.02</u> 30.99
	MPSNR b	28.41	18.04	25.80	29.29	<u>32.47</u>	31.00	23.13	30.22 32.63
	MSSIM f	0.1117	<u>0.6391</u>	0.0890	0.0535	0.7253	0.4153	0.2699	0.5942 0.5660
	MSSIM b	0.8292	0.3564	0.8538	0.8376	0.8863	0.8516	0.8517	<u>0.9000</u> 0.9331
	AUC	0.8035	0.5002	0.8004	0.5242	0.9584	0.9593	0.7956	<u>0.9756</u> 0.9861
CAMEL seq20	MPSNR f	19.97	31.06	19.59	18.77	31.00	28.50	25.63	33.55 <u>33.35</u>
	MPSNR b	30.95	19.30	28.21	28.77	30.99	30.19	26.43	38.32 <u>35.34</u>
	MSSIM f	0.0774	0.8179	0.0638	0.0559	0.5041	0.2967	0.1465	<u>0.6918</u> 0.6519
	MSSIM b	0.7373	0.1589	0.7667	0.7187	0.7938	0.7330	0.9385	0.9674 0.9499
	AUC	0.9303	0.6617	0.9412	0.5548	0.9744	0.9672	0.9873	0.9947 <u>0.9935</u>
CAMEL seq21	MPSNR f	19.99	<u>37.23</u>	19.62	18.97	31.44	28.87	19.37	37.97 34.70
	MPSNR b	31.11	19.43	28.47	29.26	31.18	30.55	19.83	<u>35.05</u> 35.53
	MSSIM f	0.0778	0.8593	0.0641	0.0556	0.3771	0.2618	0.0590	<u>0.8396</u> 0.7084
	MSSIM b	0.7311	0.1413	0.7603	0.6987	0.7818	0.7227	0.8302	<u>0.8701</u> 0.9507
	AUC	0.9542	0.7216	0.9614	0.5942	0.9885	0.9832	<u>0.9921</u>	0.9991 0.9919
Bird	MPSNR f	19.86	49.42	19.49	20.15	<u>49.16</u>	48.97	7.53	41.91 39.85
	MPSNR b	29.98	19.99	27.36	34.72	<u>34.72</u>	32.92	7.72	<u>37.52</u> 39.83
	MSSIM f	0.0311	0.9881	0.0213	0.0439	<u>0.9839</u>	0.9762	0.0046	0.9238 0.8969
	MSSIM b	0.7220	0.1496	0.7444	0.7829	<u>0.7827</u>	0.7081	0.2707	<u>0.9258</u> 0.9396
	AUC	0.7505	0.5000	0.7617	0.6808	<u>0.8336</u>	<u>0.8467</u>	0.5986	0.9047 0.7140
Cell1	MPSNR f	29.76	29.76	30.56	20.19	31.35	28.87	8.92	33.70 <u>31.87</u>
	MPSNR b	19.42	19.43	20.12	30.53	31.83	30.73	8.93	<u>34.59</u> 36.21
	MSSIM f	0.7642	0.7642	0.5536	0.0541	<u>0.6970</u>	0.3215	0.0253	0.6904 0.5652
	MSSIM b	0.0871	0.0871	0.0968	0.6456	0.7264	0.6553	0.3607	<u>0.8460</u> 0.9864
	AUC	0.5000	0.5001	0.8456	0.5074	0.7193	0.6817	0.9300	<u>0.9288</u> 0.8043
Cell2	MPSNR f	19.89	35.06	19.42	20.46	37.48	31.34	7.17	<u>36.29</u> 34.51
	MPSNR b	30.25	34.43	26.86	32.97	<u>34.54</u>	32.93	7.17	<u>40.73</u> 43.01
	MSSIM f	0.0388	<u>0.9318</u>	0.0198	0.0618	0.9372	0.4197	0.0036	0.7819 0.7290
	MSSIM b	0.6794	0.7554	0.7143	0.6858	0.7561	0.6871	0.1931	<u>0.9692</u> 0.9804
	AUC	0.7605	0.5000	0.7384	0.5175	0.9243	0.9317	0.1451	0.9787 <u>0.9359</u>

follows: let $\mathbf{B} = \mathbf{U}_B \mathbf{S}_B \mathbf{V}_B^\top$ be the singular value decomposition of \mathbf{B} , then

$$\text{prox}_{\gamma \|\cdot\|_*}(\mathbf{B}) = \mathbf{U}_B \tilde{\mathbf{S}}_\gamma \mathbf{V}_B^\top, \quad (21)$$

where $\tilde{\mathbf{S}}_\gamma$ is a diagonal matrix whose i -th element is $\max\{s_i(\mathbf{B}) - \gamma, 0\}$. The stepsize parameter γ_b is determined as $\gamma_b = 1/9$.

As a second example, let us consider static scene constraint modeling [59], which characterizes a background component as exactly static. This modeling makes an algorithm relatively efficient for low-rank modeling by imposing zero to all the values of the temporal gradient of \mathbf{b} as follows:

$$\mathbf{D}_t \mathbf{b} = \mathbf{0}. \quad (22)$$

Using this constraint is identical to adding $\iota_{\{0\}}(\mathbf{D}_t \mathbf{b})$ into the objective function. Therefore, by removing $R_0(\mathbf{b})$ and letting $K = 1$, $\mathbf{L}_1 = \mathbf{D}_t$, and $R_1 = \iota_{\{0\}}$, we can apply the static scene constraint modeling to Prob. (6). In Algorithm 2, the

steps 7, 8, 21, and 22 respectively become

$$\mathbf{b}' \leftarrow \mathbf{b}^{(l)} - \gamma_b (\mathbf{D}_t^\top \mathbf{z}_{1,1}^{(l)} + \mathbf{D}^\top \mathbf{z}_3^{(l)} + \mathbf{z}_4^{(l)}), \quad (23)$$

$$\mathbf{b}^{(l+1)} \leftarrow \mathbf{b}', \quad (24)$$

$$\mathbf{z}_{1,1}' \leftarrow \mathbf{z}_{1,1}^{(l)} + \gamma_z \mathbf{D}_t \tilde{\mathbf{b}}, \quad (25)$$

$$\mathbf{z}_{1,1}^{(l+1)} \leftarrow \mathbf{z}_{1,1}'. \quad (26)$$

The stepsize parameter γ_b is determined as $\gamma_b = 1/13$.

IV. EXPERIMENTS

To demonstrate the effectiveness of CSRFM, we perform FBS experiments on low frame-rate videos with several types of noise. In the experiments, we compare CSRFM to seven existing FBS methods: RPCA [20], GNNLSM [25], TVRPCA [28], PRPCA [29], SRTC [31], SS-RTD [32], and FactorDVP-T [19]. As the background modeling of CSRFM, we adopt the low-rank modeling (referred to as CSRFM (LR)) and the static scene constraint modeling (referred to as CSRFM (SC)), described in Section III-C.

A. Datasets

As the ground-truth IR and MS videos, we used six IR videos with static background from CAMEL Dataset⁷

⁷<https://camel.ece.gatech.edu/>

TABLE IV
MPSNR, MSSIM, AND AUC VALUES OF THE FBS RESULTS IN CASE 2.

Video	Measure	Methods								
		RPCA [20]	GNNLSM [25]	TVRPCA [28]	PRPCA [29]	SRTC [31]	SS-RTD [32]	FactorDVP-T [19]	CSRFM (LR)	CSRFM (SC)
CAMEL seq8	MPSNR f	16.44	24.18	16.24	16.12	27.45	<u>31.94</u>	20.24	31.74	32.51
	MPSNR b	29.85	15.80	27.03	28.32	29.82	<u>31.18</u>	19.99	31.10	32.97
	MSSIM f	0.0482	<u>0.7639</u>	0.0437	0.0256	0.4597	0.2961	0.0845	0.7842	0.6912
	MSSIM b	0.7755	0.1607	0.8055	0.7533	0.7740	0.7788	0.8533	<u>0.8603</u>	0.9030
	AUC	0.8732	0.5045	0.8948	0.5579	0.9711	0.9787	0.9715	0.9972	<u>0.9921</u>
CAMEL seq10	MPSNR f	16.22	19.12	15.95	15.86	22.84	27.30	21.09	31.81	<u>31.52</u>
	MPSNR b	30.18	17.54	27.47	30.03	30.19	29.97	21.99	32.96	<u>32.24</u>
	MSSIM f	0.0597	0.2146	0.0520	0.0213	0.1875	0.2934	0.1482	0.6470	<u>0.6116</u>
	MSSIM b	0.7273	0.1609	0.7630	0.7256	0.7470	0.7338	0.7315	<u>0.8964</u>	0.9396
	AUC	0.7805	0.5078	0.7776	0.5139	0.9049	0.9111	0.6578	0.9783	<u>0.9694</u>
CAMEL seq17	MPSNR f	16.06	24.97	15.84	15.73	25.11	28.30	15.77	<u>30.11</u>	31.13
	MPSNR b	28.48	15.40	25.80	30.17	<u>30.83</u>	31.17	15.42	28.12	30.42
	MSSIM f	0.0595	0.6672	0.0495	0.0232	0.4386	0.3955	0.0447	<u>0.6171</u>	0.5531
	MSSIM b	0.8250	0.2563	0.8471	0.8304	0.8299	0.8405	0.8022	<u>0.8526</u>	0.8974
	AUC	0.7370	0.5000	0.7345	0.5162	0.9279	0.9290	0.5488	<u>0.9573</u>	0.9694
CAMEL seq18	MPSNR f	16.10	22.94	15.83	15.50	24.71	27.63	17.42	<u>29.39</u>	30.48
	MPSNR b	27.99	15.19	25.42	28.89	30.38	30.72	17.10	28.29	<u>30.66</u>
	MSSIM f	0.0699	0.6391	0.0599	0.0224	0.4353	0.3919	0.0766	0.5521	<u>0.6143</u>
	MSSIM b	0.8183	0.2468	0.8412	0.8253	0.8260	0.8419	<u>0.8437</u>	0.8288	0.9004
	AUC	0.7766	0.5002	0.7706	0.5219	0.9335	0.9525	0.6261	<u>0.9729</u>	0.9836
CAMEL seq20	MPSNR f	16.19	18.59	15.95	15.75	22.34	27.93	28.63	33.51	<u>33.25</u>
	MPSNR b	30.46	18.57	27.56	28.35	29.03	29.86	32.17	34.69	<u>33.99</u>
	MSSIM f	0.0491	0.2640	0.0427	0.0264	0.1144	0.2840	0.2481	0.7701	<u>0.6491</u>
	MSSIM b	0.7189	0.1394	0.7514	0.7005	0.7375	0.7128	0.8703	<u>0.9408</u>	0.9479
	AUC	0.9058	0.6465	0.9170	0.5552	0.9375	0.9612	0.9903	0.9981	<u>0.9929</u>
CAMEL seq21	MPSNR f	16.03	18.06	15.77	15.59	21.27	28.35	33.20	35.56	<u>34.46</u>
	MPSNR b	30.56	18.75	27.72	28.71	28.70	30.17	34.41	30.80	<u>33.00</u>
	MSSIM f	0.0512	0.2612	0.0444	0.0268	0.0978	0.2492	0.5148	0.7670	<u>0.6755</u>
	MSSIM b	0.7085	0.1276	0.7426	0.6764	0.7280	0.6978	0.8302	0.9574	<u>0.9513</u>
	AUC	0.9308	0.6616	0.9379	0.5874	0.9577	0.9795	<u>0.9954</u>	0.9965	0.9830
Bird	MPSNR f	15.85	19.91	15.67	15.93	51.09	<u>48.80</u>	11.08	48.44	43.47
	MPSNR b	29.44	18.06	26.75	32.41	29.76	32.46	11.03	<u>38.09</u>	41.77
	MSSIM f	0.0155	0.4576	0.0107	0.0203	0.9892	<u>0.9759</u>	0.0123	<u>0.9759</u>	0.9506
	MSSIM b	0.6999	0.1200	0.7237	0.6854	0.5952	0.6867	0.6999	<u>0.9675</u>	0.9678
	AUC	0.7439	0.5036	0.7560	0.7187	0.4393	<u>0.9212</u>	0.5951	0.9835	0.7703
Cell1	MPSNR f	29.76	29.76	30.19	16.79	26.72	28.63	12.04	33.36	<u>32.09</u>
	MPSNR b	16.30	16.30	16.35	30.24	30.29	30.47	12.18	38.85	<u>36.86</u>
	MSSIM f	<u>0.7642</u>	<u>0.7642</u>	0.7676	0.0248	0.3085	0.3088	0.0318	0.6726	0.5809
	MSSIM b	0.0486	0.0486	0.0488	0.6202	0.6230	0.6317	0.7034	<u>0.9679</u>	0.9915
	AUC	0.5000	0.5000	0.7719	0.5073	0.6626	0.6698	<u>0.8923</u>	0.9228	0.8274
Cell2	MPSNR f	16.54	33.48	16.28	16.91	29.69	30.93	6.68	<u>37.90</u>	38.23
	MPSNR b	29.75	16.54	26.39	32.35	32.01	32.42	6.87	<u>39.12</u>	41.46
	MSSIM f	0.0203	0.9232	0.0118	0.0273	0.5196	0.3977	0.0036	<u>0.8217</u>	0.8179
	MSSIM b	0.6570	0.0618	0.6971	0.6553	0.6364	0.6615	0.1348	0.9782	<u>0.9779</u>
	AUC	0.7332	0.5019	0.7109	0.5125	0.9069	0.9235	0.1345	<u>0.9844</u>	0.9856

(cropped into a size of $128 \times 128 \times 30$) [60], [61], one IR video from Bird Dataset⁸ (cropped into a size of 200×200 and sampled 30 frames) [62], one MS video from T cell signaling proteins 3D confocal microscope movies⁹ (cropped into a size of 128×128 and sampled 30 frames), and one MS video from Cell Tracking Challenge Datasets¹⁰ (cropped into a size of 200×200 and sampled 30 frames). We sampled frames every few frames to compare performance in low frame rate situations, and normalized pixel values into $[0, 1]$. By applying RPCA with the recommended parameter value to these ground-truth videos, the pseudo ground-truth background and foreground components were generated. In addition, through threshold processing on the pseudo ground-truth foreground components, we obtain the pseudo ground-truth foreground maps for calculating the area under the receiver operating characteristic curve (AUC) (described in Section IV-B3). Fig. 2 shows the frames of the ground-truth videos and the pseudo ground-truth foreground maps.

B. Experimental Setup

1) *Noise Setup*: We consider the following cases of noise.

Case 1 (Gaussian noise): The observed HS image is contaminated by white Gaussian noise with the standard deviation $\sigma = 0.1$.

Case 2 (Gaussian noise + salt-and-pepper noise): The observed HS image is contaminated by white Gaussian noise with the standard deviation $\sigma = 0.1$ and salt-and-pepper noise with the rate $p_s = 0.05$.

Case 3 (Gaussian noise + salt-and-pepper noise + stripe noise): The observed HS image is contaminated by white Gaussian noise with the standard deviation $\sigma = 0.1$ and salt-and-pepper noise with the rate $p_s = 0.05$. In addition, the observed HS image is corrupted by vertical stripe noise whose intensity is random in the range $[-0.2, 0.2]$. We only added time-invariant stripe noise because the stripe location of video data often does not change over time [63].

2) *Parameter Setup*: The parameters of existing methods and CSRFM were adjusted in the ranges shown in Tab. I to minimize the recovery error of objects of a foreground component \mathbf{f} , a background component \mathbf{b} , and a clean video $\mathbf{u} = \mathbf{f} + \mathbf{b}$. Specifically, we determined them to take small

⁸<https://universe.roboflow.com/antiuv-9-aniket/bird-6le8u>

⁹https://kilthub.cmu.edu/articles/dataset/T_cell_signaling_proteins_3D_confocal_microscope_movies/9963566

¹⁰<http://celltrackingchallenge.net/2d-datasets/>

TABLE V
MPSNR, MSSIM, AND AUC VALUES OF THE FBS RESULTS IN CASE 3.

Video	Measure	Methods							
		RPCA [20]	GNNLSM [25]	TVRPCA [28]	PRPCA [29]	SRTC [31]	SS-RTD [32]	FactorDVP-T [19]	CSRFM (LR) CSRFM (SC)
CAMEL seq8	MPSNR f	16.44	24.18	16.24	16.13	27.33	31.95	27.93	31.64 32.08
	MPSNR b	24.26	15.34	23.60	23.29	23.83	23.92	23.74	27.98 27.92
	MSSIM f	0.0484	0.7638	0.0440	0.0256	0.4528	0.2952	0.3197	0.7557 0.6288
	MSSIM b	0.4987	0.1472	0.5128	0.4865	0.4844	0.4913	0.4991	0.7263 0.7351
	AUC	0.8739	0.5044	0.8957	0.5572	0.9695	0.9808	0.9783	0.9969 0.9918
CAMEL seq10	MPSNR f	16.15	19.12	15.89	15.78	22.63	27.17	25.46	30.84 29.49
	MPSNR b	22.65	16.36	22.24	22.17	22.27	22.11	27.04	29.02 28.79
	MSSIM f	0.0604	0.2233	0.0534	0.0207	0.1837	0.2714	0.4240	0.6117 0.5442
	MSSIM b	0.3809	0.1337	0.3955	0.3671	0.3739	0.3669	0.7371	0.7878 0.8213
	AUC	0.7789	0.5081	0.7769	0.5134	0.9003	0.9092	0.4695	0.9682 0.9341
CAMEL seq17	MPSNR f	16.03	24.97	15.80	15.69	25.01	28.31	21.44	29.82 30.99
	MPSNR b	24.35	15.02	23.35	24.50	24.77	24.73	20.07	27.52 27.42
	MSSIM f	0.0589	0.6670	0.0489	0.0228	0.4305	0.3958	0.1228	0.5816 0.5529
	MSSIM b	0.6337	0.2373	0.6452	0.6275	0.6314	0.6342	0.6286	0.8205 0.8149
	AUC	0.7411	0.5001	0.7378	0.5209	0.9223	0.9313	0.7292	0.9451 0.9670
CAMEL seq18	MPSNR f	16.04	22.94	15.78	15.43	24.56	27.60	19.71	29.05 30.46
	MPSNR b	23.46	14.75	22.45	23.58	24.05	24.02	18.74	26.98 27.10
	MSSIM f	0.0691	0.6391	0.0590	0.0226	0.4271	0.3866	0.1080	0.5317 0.5667
	MSSIM b	0.6077	0.2252	0.6195	0.5991	0.6066	0.6093	0.5663	0.7855 0.7769
	AUC	0.7778	0.5002	0.7730	0.5261	0.9354	0.9523	0.7053	0.9689 0.9828
CAMEL seq20	MPSNR f	16.16	18.52	15.91	15.71	22.18	27.84	26.73	32.93 31.81
	MPSNR b	24.38	17.75	23.66	23.31	23.58	23.70	24.19	30.27 30.72
	MSSIM f	0.0497	0.2581	0.0433	0.0262	0.1087	0.2727	0.2391	0.6917 0.6202
	MSSIM b	0.3901	0.1214	0.4054	0.3637	0.3752	0.3690	0.4032	0.8077 0.8802
	AUC	0.9037	0.6500	0.9157	0.5552	0.9333	0.9596	0.9652	0.9892 0.9827
CAMEL seq21	MPSNR f	16.00	18.14	15.76	15.57	21.36	28.06	30.59	37.16 35.54
	MPSNR b	24.47	17.53	24.20	22.67	22.64	22.91	23.65	29.75 31.89
	MSSIM f	0.0506	0.2672	0.0444	0.0259	0.0972	0.2179	0.3614	0.8226 0.7141
	MSSIM b	0.3431	0.1034	0.3603	0.3080	0.3220	0.3137	0.3378	0.6790 0.9347
	AUC	0.9290	0.6458	0.9362	0.5861	0.9552	0.9723	0.9790	0.9989 0.9943
Bird	MPSNR f	15.81	19.79	15.64	15.89	51.09	48.57	7.40	40.81 42.75
	MPSNR b	23.41	17.16	22.59	23.79	23.68	23.79	7.30	29.58 29.97
	MSSIM f	0.0155	0.4497	0.0107	0.0203	0.9892	0.9745	0.0034	0.9304 0.9429
	MSSIM b	0.3597	0.1024	0.3696	0.3442	0.3314	0.3447	0.1085	0.7676 0.7894
	AUC	0.7276	0.5100	0.7418	0.7049	0.3660	0.8811	0.5867	0.9241 0.7736
Cell1	MPSNR f	29.76	29.76	30.15	16.76	26.34	28.60	14.91	33.13 31.89
	MPSNR b	15.72	15.72	15.79	23.58	23.58	23.59	15.13	29.40 38.85
	MSSIM f	0.7642	0.7642	0.7585	0.0247	0.3030	0.3114	0.0287	0.6760 0.5860
	MSSIM b	0.0421	0.0421	0.0423	0.2478	0.2492	0.2496	0.5513	0.7176 0.9963
	AUC	0.5000	0.5000	0.7473	0.5044	0.6613	0.6732	0.7499	0.9132 0.8185
Cell2	MPSNR f	16.50	28.23	16.25	16.89	28.93	30.87	22.71	37.30 35.81
	MPSNR b	23.84	16.16	22.57	24.64	24.60	24.61	21.13	31.80 32.35
	MSSIM f	0.0197	0.8270	0.0117	0.0274	0.4970	0.3944	0.0383	0.7994 0.7857
	MSSIM b	0.3284	0.0572	0.3434	0.3151	0.3106	0.3154	0.4254	0.8318 0.8600
	AUC	0.7313	0.5035	0.7076	0.5150	0.9099	0.9231	0.3409	0.9825 0.9347

values in measure calculated by the following equation:

$$\sum_{i=1}^{n_1 n_2 n_3} |\bar{u}_i - \mu_{\bar{u}}| (u_i - \bar{u}_i)^2 + |\bar{f}_i - \mu_{\bar{f}}| (f_i - \bar{f}_i)^2 + |\bar{b}_i - \mu_{\bar{b}}| (b_i - \bar{b}_i)^2, \quad (27)$$

where $\mu_{\bar{u}}$, $\mu_{\bar{f}}$, and $\mu_{\bar{b}}$ are the mean values of \bar{u} , \bar{f} , and \bar{b} , respectively. The reason for weighting by the absolute values of the difference between pixel values and means, rather than the absolute values of pixel values, is to enable appropriate evaluation even for videos that have high-intensity pixel values in regions where any objects do not exist. Specifically, since MS videos (cell 1 and cell 2) have such regions, the measure with weights by the absolute values do not allow us to evaluate the object recovery performance. To avoid this, we used the measure in Eq. (27). The parameter λ_1 was determined by 0.05 to achieve good performance, with reference to Ref. [47]. For the parameters η_s and ε in (6), we set them as $\eta_s = 0.5p_s n_1 n_2 n_3$ and $\varepsilon = 0.9\sigma\sqrt{(1-p_s)n_1 n_2 n_3}$, respectively. The parameter η_f , the number of filters D , and the size of filters were roughly determined from the intensity, the number, and the size of the foreground objects, as shown in Tab. II. For Algorithm 1, we set the maximum iterations to 300 and the stopping criterion to $\|\mathbf{b}^{(n+1)} - \mathbf{b}^{(n)}\|_2 / \|\mathbf{b}^{(n)}\|_2 \leq 10^{-5}$ and $\|\mathbf{f}^{(n+1)} - \mathbf{f}^{(n)}\|_2 / \|\mathbf{f}^{(n)}\|_2 \leq 10^{-5}$. Moreover, we set

the maximum iterations of Algorithms 2 and 3 to 500 and 10, respectively. After obtaining the dictionaries, we finally estimated \mathbf{f} and \mathbf{b} using Algorithm 2 with 20000 iterations.

3) *Evaluation Metric*: For the quality measures, we used the mean of the peak-signal-to-noise ratio (MPSNR) [dB]:

$$\text{MPSNR}(\mathbf{q}, \bar{\mathbf{q}}) := \frac{1}{n_3} \sum_{k=1}^{n_3} 10 \log_{10} \frac{n_1 n_2}{\|\mathbf{q}_{n_3} - \bar{\mathbf{q}}_{n_3}\|_2^2}, \quad (28)$$

and the mean of structural similarity (MSSIM) [64]:

$$\text{MSSIM}(\mathbf{q}, \bar{\mathbf{q}}) := \frac{1}{n_3} \sum_{k=1}^{n_3} \text{SSIM}(\mathbf{q}_k, \bar{\mathbf{q}}_k), \quad (29)$$

for $\mathbf{q} = \mathbf{f}$ and $\mathbf{q} = \mathbf{b}$, where \mathbf{q}_k is the k -th frame of a video to be evaluated and $\bar{\mathbf{q}}_k$ is a reference frame to \mathbf{q}_k . The higher the MPSNR and MSSIM values are, the better the estimation performance. In addition, we adopted AUC [65], which is the area under receiver operating characteristic curve with the true positive rate on the vertical axis and the false positive rate plotted on the horizontal axis. The closer the AUC value is to 1, the better the foreground estimation performance.

C. Experimental Results and Discussion

Tables III, IV, and V show the MPSNR, MSSIM, and AUC results in Case 1, Case 2, and Case 3, respectively.

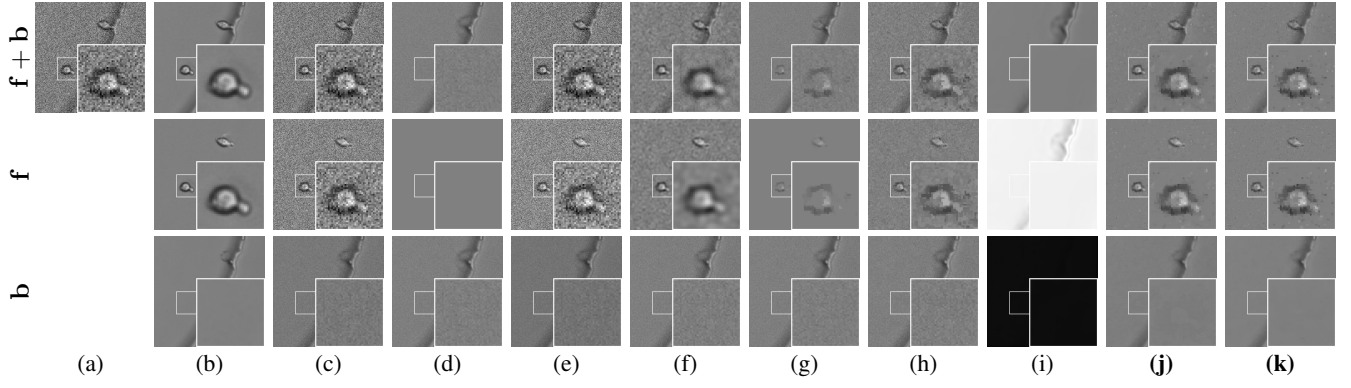


Fig. 3. FBS results for *Cell2* in Case 1. (a): Noisy frame. (b): Ground-truth frame. (c): RPCA [20]. (d): GNNLSM [25]. (e): TVRPCA [28]. (f): PRPCA [29]. (g): SRTC [31]. (h): SS-RTD [32]. (i): FactorDVP-T [19]. (j): **CSRFM (LR)**. (k): **CSRFM (SC)**.

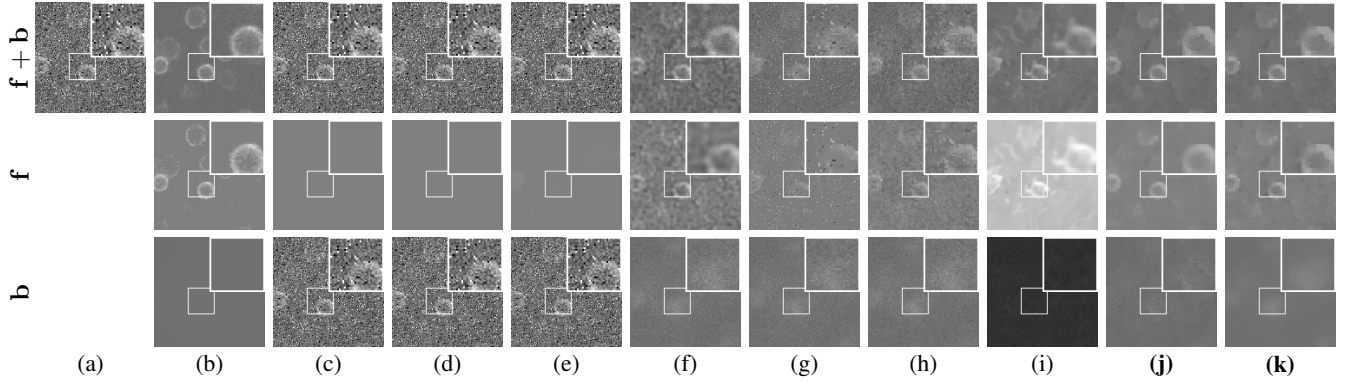


Fig. 4. FBS results for *Cell1* in Case 2. (a): Noisy frame. (b): Ground-truth frame. (c): RPCA [20]. (d): GNNLSM [25]. (e): TVRPCA [28]. (f): PRPCA [29]. (g): SRTC [31]. (h): SS-RTD [32]. (i): FactorDVP-T [19]. (j): **CSRFM (LR)**. (k): **CSRFM (SC)**.

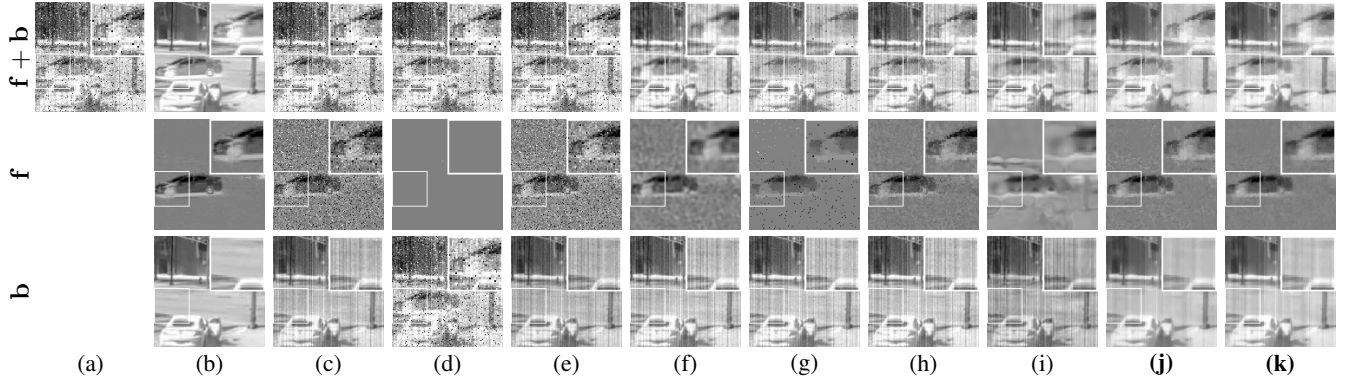


Fig. 5. FBS results for *CAMEL seq17* in Case 3. (a): Noisy frame. (b): Ground-truth frame. (c): RPCA [20]. (d): GNNLSM [25]. (e): TVRPCA [28]. (f): PRPCA [29]. (g): SRTC [31]. (h): SS-RTD [32]. (i): FactorDVP-T [19]. (j): **CSRFM (LR)**. (k): **CSRFM (SC)**.

The best and second-best values are highlighted in bold and underlined, respectively. RPCA, GNNLSM, TVRPCA, and PRPCA produced worse results than the other methods in almost all cases. GNNLSM resulted in the best/second-best MPSNR f and MSSIM f values for some videos, but its ACU values are close to 0.5. This indicates that it does not adequately estimate foreground components, although its performance appears to be good in MPSNR f and MSSIM f . SRTC and SS-RTD performed better than the other existing methods. However, they do not adequately model multiple types of noise (particularly sparse and stripe noise), reducing the capability of FBS in Cases 2 and 3. FactorDVP-T did not

perform well overall. In particular, its performance is degraded for *Bird*, *Cell1*, and *Cell2*, which contain small foreground objects. In contrast, CSRFM achieved best/second-best results in almost all cases.

Figures 3, 4, and 5 depict the FBS results for *Cell2* in Case 1, *Cell1* in Case 2, and for *CAMEL seq17* in Case 3, respectively. Figure 6 visualize some bases d obtained in the FBS process of CSRFM. RPCA and GNNLSM only captured the sparsity of the foreground components and thus did not separate the foreground components from noise (Figs. 3, 4, and 5 (c) and (d)). TVRPCA also failed to separate them (Figs. 3, 4, and 5 (e)) because it does not explicitly model

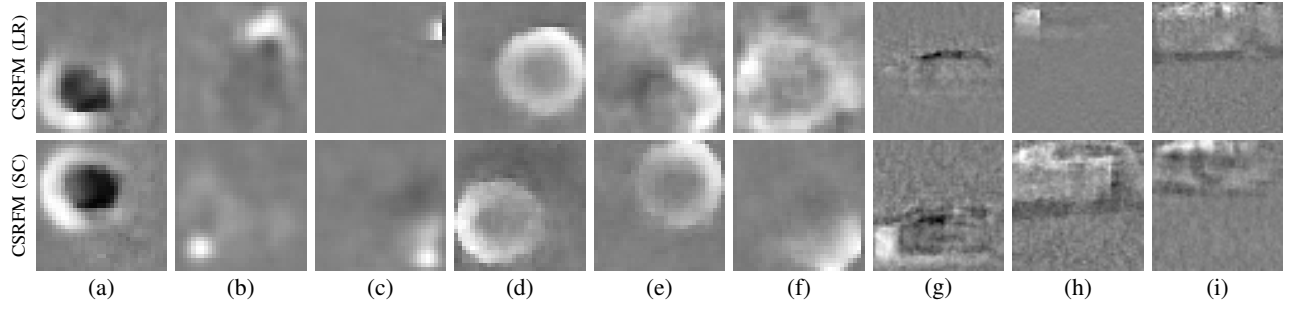


Fig. 6. Some bases \mathbf{d} obtained in the FBS process of CSRFBM. (a)-(c): *Cell2* in Case 1. (d)-(f): *Cell1* in Case 2. (g)-(i): *CAMEL seq17* in Case 3.

TABLE VI
MPSNR, MSSIM, AND AUC VALUES OF THE ABLATION EXPERIMENTS.

Video	Measure	LR (Left: without CSR, Right: with CSR)						SC (Left: without CSR, Right: with CSR)					
		Case 1		Case 2		Case 3		Case 1		Case 2		Case 3	
		–	✓	–	✓	–	✓	–	✓	–	✓	–	✓
<i>CAMEL seq8</i>	MPSNR f	31.66	32.32	31.27	31.74	30.74	31.64	30.85	32.68	30.88	32.51	30.15	32.08
	MPSNR b	31.80	30.78	30.27	31.10	28.69	27.98	32.17	34.87	30.36	32.97	29.01	27.92
	MSSIM f	0.6107	0.6546	0.6194	0.7842	0.5967	0.7557	0.5618	0.6314	0.5850	0.6912	0.5616	0.6288
	MSSIM b	0.8693	0.9443	0.8381	0.8603	0.7946	0.7263	0.8894	0.9374	0.8455	0.9030	0.8211	0.7351
	AUC	0.9852	0.9867	0.9840	0.9972	0.9780	0.9969	0.9775	0.9921	0.9799	0.9921	0.9688	0.9918
<i>CAMEL seq10</i>	MPSNR f	31.39	31.17	31.50	31.81	30.19	30.84	29.88	31.11	30.39	31.52	29.19	29.49
	MPSNR b	33.36	36.32	32.92	32.96	28.98	29.02	32.44	32.72	31.44	32.24	28.39	28.79
	MSSIM f	0.6162	0.6211	0.6344	0.6470	0.5864	0.6117	0.5292	0.5763	0.5967	0.6116	0.5343	0.5442
	MSSIM b	0.8992	0.9408	0.8965	0.8964	0.7908	0.7878	0.9394	0.9549	0.9150	0.9396	0.8153	0.8213
	AUC	0.9737	0.9659	0.9753	0.9783	0.9585	0.9682	0.9514	0.9626	0.9556	0.9694	0.9260	0.9341
<i>CAMEL seq17</i>	MPSNR f	29.94	30.54	29.59	30.11	29.02	29.82	29.71	31.45	29.55	31.13	28.84	30.99
	MPSNR b	29.51	30.76	28.18	28.12	26.94	27.52	30.31	32.42	28.52	30.42	27.33	27.42
	MSSIM f	0.5578	0.6018	0.5504	0.6171	0.5342	0.5816	0.5115	0.5708	0.5153	0.5531	0.4980	0.5529
	MSSIM b	0.8636	0.9023	0.8238	0.8526	0.7948	0.8205	0.8900	0.9350	0.8400	0.8974	0.8215	0.8149
	AUC	0.9539	0.9612	0.9506	0.9573	0.9393	0.9451	0.9420	0.9711	0.9419	0.9694	0.9288	0.9670
<i>CAMEL seq18</i>	MPSNR f	29.52	30.02	29.10	29.39	28.36	29.05	29.52	30.99	29.15	30.48	28.39	30.46
	MPSNR b	29.78	30.22	28.33	28.29	26.93	26.98	30.48	32.63	28.61	30.66	27.25	27.10
	MSSIM f	0.5427	0.5942	0.5350	0.5521	0.5026	0.5317	0.5088	0.5660	0.5010	0.6143	0.4771	0.5667
	MSSIM b	0.8697	0.9000	0.8280	0.8288	0.7853	0.7855	0.8872	0.9331	0.8384	0.9004	0.7975	0.7769
	AUC	0.9724	0.9756	0.9673	0.9729	0.9595	0.9689	0.9713	0.9861	0.9665	0.9836	0.9593	0.9828
<i>CAMEL seq20</i>	MPSNR f	33.36	33.55	33.42	33.51	32.39	32.93	32.10	33.35	33.11	33.25	31.66	31.81
	MPSNR b	36.84	38.32	36.11	34.69	31.34	30.27	35.14	35.34	33.90	33.99	30.60	30.72
	MSSIM f	0.6779	0.6918	0.7118	0.7701	0.6654	0.6917	0.6002	0.6519	0.6469	0.6491	0.6140	0.6202
	MSSIM b	0.9424	0.9674	0.9456	0.9408	0.8614	0.8077	0.9644	0.9499	0.9476	0.9479	0.8780	0.8802
	AUC	0.9948	0.9947	0.9957	0.9981	0.9909	0.9892	0.9868	0.9935	0.9922	0.9929	0.9812	0.9827
<i>CAMEL seq21</i>	MPSNR f	34.73	37.97	35.43	35.56	33.60	37.16	32.03	34.70	34.02	34.46	31.99	35.54
	MPSNR b	36.83	35.05	36.92	30.80	31.08	29.75	34.40	35.53	32.84	33.00	29.35	31.89
	MSSIM f	0.7366	0.8396	0.7619	0.7670	0.7231	0.8226	0.6058	0.7084	0.6730	0.6755	0.6375	0.7141
	MSSIM b	0.9281	0.8701	0.9443	0.9574	0.8119	0.6790	0.9660	0.9507	0.9510	0.9513	0.8304	0.9347
	AUC	0.9953	0.9991	0.9958	0.9965	0.9921	0.9989	0.9758	0.9919	0.9803	0.9830	0.9610	0.9943
<i>bird1</i>	MPSNR f	41.28	41.91	41.13	48.44	39.94	40.81	39.29	39.85	41.60	43.47	42.32	42.75
	MPSNR b	35.31	37.52	37.08	38.09	29.59	29.58	35.41	39.83	41.45	41.77	28.94	29.97
	MSSIM f	0.9186	0.9238	0.9327	0.9759	0.9230	0.9304	0.8869	0.8969	0.9395	0.9506	0.9357	0.9429
	MSSIM b	0.8863	0.9258	0.9484	0.9675	0.7672	0.7676	0.8115	0.9396	0.9633	0.9678	0.7045	0.7894
	AUC	0.8992	0.9047	0.9063	0.9835	0.8881	0.9241	0.6544	0.7140	0.7644	0.7703	0.7254	0.7736
<i>cell1</i>	MPSNR f	31.72	33.70	32.43	33.36	31.04	33.13	30.87	31.87	31.57	32.09	30.33	31.89
	MPSNR b	35.68	34.59	38.97	38.85	30.51	29.40	36.05	36.21	36.13	36.86	30.86	38.85
	MSSIM f	0.5856	0.6904	0.6352	0.6726	0.5632	0.6760	0.5448	0.5652	0.5804	0.5809	0.5266	0.5860
	MSSIM b	0.9548	0.8460	0.9908	0.9679	0.8326	0.7176	0.9864	0.9864	0.9858	0.9915	0.8680	0.9963
	AUC	0.8098	0.9288	0.8669	0.9228	0.7724	0.9132	0.7676	0.8043	0.8109	0.8274	0.7129	0.8185
<i>cell2</i>	MPSNR f	36.68	36.29	37.60	37.90	36.43	37.30	33.74	34.51	37.22	38.23	35.28	35.81
	MPSNR b	38.56	40.73	40.76	39.12	31.88	31.80	43.61	43.01	41.51	41.46	32.17	32.35
	MSSIM f	0.7799	0.7819	0.8075	0.8217	0.7854	0.7994	0.7057	0.7290	0.8019	0.8179	0.7776	0.7857
	MSSIM b	0.9353	0.9692	0.9744	0.9782	0.8363	0.8318	0.9828	0.9804	0.9769	0.9779	0.8531	0.8600
	AUC	0.9807	0.9787	0.9857	0.9844	0.9728	0.9825	0.9064	0.9359	0.9839	0.9856	0.9261	0.9347

noise. PRPCA, SRTC, and SS-RTD reduced the effect of noise through the total variation regularization, but their estimated components remain noisy or oversmoothed (Figs. 3, 4, and 5 (f), (g), and (h)). This is because they cannot capture the specific structures (e.g., edges and shapes) of temporally discontinuous foreground objects in low frame-rate videos. The results of FactorDVP-T were unstable, as it completely eliminated foreground components (Fig. 3 (i)), generated shapes that do not exist in the ground-truth foreground component (Fig. 4 (i)), generated brighter/darker frames than the original

frames (Figs. 3 and 4 (i)), and distorted objects (Fig. 5 (i)). This is because FactorDVP-T does not take into account general features such as sparsity and piecewise smoothness in FBS. In contrast, due to the CSR-based foreground modeling, CSRFBM recovered the foreground objects (Figs. 3, 4, and 5 (j) and (k)) by referring to the bases (Figs. 6) simultaneously estimated in the FBS process. In addition, our model removed noise due to explicit noise modeling. These facts show the effectiveness of CSRFBM.

D. Ablation Experiments

To demonstrate the contribution of the CSR-based foreground modeling, we compared CSRFM performance with the performance when the CSR-based foreground modeling was removed. Specifically, we remove the first term, the second term, and the fifth constraint from Eq. (6). The parameters were set to the same as in CSRFM.

Table VI shows the MPSNR, MSSIM, and AUC results in all cases. The higher value of CSRFM without CSR or CSRFM with CSR is highlighted in bold. CSRFM with CSR was superior to CSRFM without CSR particularly in MPSNR f, MSSIM f, and AUC. This implies that CSR improves to capture the nature of foreground components.

V. CONCLUSION

We have proposed CSRFM, which adaptively captures the specific structures of foreground objects by CSR and promotes the sparsity and piecewise smoothness of foreground components by certain functions. Thanks to these foreground modeling, CSRFM has adequately separated the foreground and background components from noisy and low frame-rate videos. In addition, we have formulated the FBS as a constrained multiconvex optimization problem and developed an ALM algorithm to solve the problem. The experimental results have demonstrated the superiority of our model over existing foreground models.

REFERENCES

- [1] "Decomposition into low-rank plus additive matrices for background/foreground separation: A review for a comparative evaluation with a large-scale dataset," *Comput. Sci. Rev.*, vol. 23, pp. 1–71, 2017.
- [2] T. Bouwmans, S. Javed, H. Zhang, Z. Lin, and R. Otazo, "On the applications of robust PCA in image and video processing," *Proc. IEEE*, vol. 106, no. 8, pp. 1427–1457, Aug. 2018.
- [3] S.-C. Huang, "An advanced motion detection algorithm with video quality analysis for video surveillance systems," *IEEE Trans. Circuits. Syst. Video Technol.*, vol. 21, no. 1, pp. 1–14, Jan. 2011.
- [4] X. Zhou, C. Yang, and W. Yu, "Moving object detection by detecting contiguous outliers in the low-rank representation," *IEEE Trans. Pattern Anal. Mach. Intell.*, vol. 35, no. 3, pp. 597–610, Mar. 2013.
- [5] "Infrared small target and background separation via column-wise weighted robust principal component analysis," *Infr. Phys. Technol.*, vol. 77, pp. 421–430, 2016.
- [6] L. Deng, J. Song, G. Xu, and H. Zhu, "When infrared small target detection meets tensor ring decomposition: A multiscale morphological framework," *IEEE Trans. Aerosp. Electron. Syst.*, vol. 58, no. 4, pp. 3162–3176, Aug. 2022.
- [7] A. Sobral and A. Vacavant, "A comprehensive review of background subtraction algorithms evaluated with synthetic and real videos," *Comput. Vis. Image Understanding*, vol. 122, pp. 4–21, May 2014.
- [8] Z. Li, Y. Wang, Q. Zhao, S. Zhang, and D. Meng, "A tensor-based online RPCA model for compressive background subtraction," *IEEE Trans. Neural Netw. Learn. Syst.*, vol. 34, no. 12, pp. 10 668–10 682, 2023.
- [9] T. Vicar, J. Balvan, J. Jaros, F. Jug, R. Kolar, M. Masarik, and J. Gumulec, "Cell segmentation methods for label-free contrast microscopy: review and comprehensive comparison," *BMC Bioinf.*, vol. 20, no. 1, p. 360, Dec. 2019.
- [10] W. Meinel, J.-C. Olivo-Marin, and E. D. Angelini, "Denoising of microscopy images: A review of the state-of-the-art, and a new sparsity-based method," *IEEE Trans. Image Process.*, vol. 27, no. 8, pp. 3842–3856, 2018.
- [11] "Removing striping artifacts in light-sheet fluorescence microscopy: a review," *Prog. Biophys. Mol. Biol.*, vol. 168, pp. 52–65, 2022, the Resolution Revolution: Fluorescence Microscopy of Biological Samples from Micro to Meso.
- [12] Q. Weng, "Thermal infrared remote sensing for urban climate and environmental studies: Methods, applications, and trends," *ISPRS J. Photogramm. Remote Sens.*, vol. 64, no. 4, pp. 335–344, 2009.
- [13] J. W. Lichtman and J.-A. Conchello, "Fluorescence microscopy," *Nature Methods*, vol. 2, no. 12, pp. 910–919, 2005.
- [14] "Background and foreground disentangled generative adversarial network for scene image synthesis," *Computers & Graphics*, vol. 97, pp. 54–66, 2021.
- [15] M. Sultana, A. Mahmood, T. Bouwmans, M. H. Khan, and S. K. Jung, "Background/foreground separation: Guided attention based adversarial modeling (GAAM) versus robust subspace learning methods," in *IEEE Int. Conf. Comput. Vis. (ICCV)*, Oct. 2021, pp. 181–188.
- [16] "Multi-scale foreground-background separation for light field depth estimation with deep convolutional networks," *Pattern Recognition Letters*, vol. 171, pp. 138–147, 2023.
- [17] M. Dombrowski, H. Reynaud, M. Baugh, and B. Kainz, "Foreground-background separation through concept distillation from generative image foundation models," in *IEEE Int. Conf. Comput. Vis. (ICCV)*, Oct. 2023, pp. 988–998.
- [18] Y. Zhao, D. Luo, F. Wang, H. Gao, M. Ye, and C. Zhu, "End-to-end compression for surveillance video with unsupervised foreground-background separation," *IEEE Trans. Broadcast.*, vol. 69, no. 4, pp. 966–978, 2023.
- [19] Y.-C. Miao, X.-L. Zhao, J.-L. Wang, X. Fu, and Y. Wang, "Snapshot compressive imaging using domain-factorized deep video prior," *IEEE Trans. Comput. Imag.*, vol. 10, pp. 93–102, 2024.
- [20] E. J. Candes, X. Li, and J. Wright, "Robust principal component analysis?" *J. ACM*, vol. 58, no. 3, pp. 11:1–11:37, Jun. 2011.
- [21] S. Prativadibhayankaram, H. V. Luong, T. H. Le, and A. Kaup, "Compressive online video background-foreground separation using multiple prior information and optical flow," *J. Imag.*, vol. 4, no. 7, 2018.
- [22] C. Lu, J. Feng, Y. Chen, W. Liu, Z. Lin, and S. Yan, "Tensor robust principal component analysis with a new tensor nuclear norm," *IEEE Trans. Pattern Anal. Mach. Intell.*, vol. 42, no. 4, pp. 925–938, Apr. 2020.
- [23] Y. Yang, Z. Yang, J. Li, and L. Fan, "Foreground-background separation via generalized nuclear norm and structured sparse norm based low-rank and sparse decomposition," *IEEE Access*, vol. 8, pp. 84 217–84 229, 2020.
- [24] Y. Wang, H. Wei, X. Ding, and J. Tao, "Video background/foreground separation model based on non-convex rank approximation RPCA and superpixel motion detection," *IEEE Access*, vol. 8, pp. 157 493–157 503, 2020.
- [25] "Generalized nuclear norm and Laplacian scale mixture based low-rank and sparse decomposition for video foreground-background separation," *Signal Process.*, vol. 172, p. 107527, 2020.
- [26] W. Cao, Y. Wang, J. Sun, D. Meng, C. Yang, A. Cichocki, and Z. Xu, "Total variation regularized tensor RPCA for background subtraction from compressive measurements," *IEEE Trans. Image Process.*, vol. 25, no. 9, pp. 4075–4090, 2016.
- [27] S. Javed, A. Mahmood, T. Bouwmans, and S. K. Jung, "Background-foreground modeling based on spatiotemporal sparse subspace clustering," *IEEE Trans. Image Process.*, vol. 26, no. 12, pp. 5840–5854, 2017.
- [28] X. Cao, L. Yang, and X. Guo, "Total variation regularized RPCA for irregularly moving object detection under dynamic background," *IEEE Trans. Cybern.*, vol. 46, no. 4, pp. 1014–1027, Apr. 2016.
- [29] B. E. Moore, C. Gao, and R. R. Nadakuditi, "Panoramic robust PCA for foreground-background separation on noisy, free-motion camera video," *IEEE Trans. Comput. Imag.*, vol. 5, no. 2, pp. 195–211, Jun. 2019.
- [30] S. Javed, A. Mahmood, S. Al-Maadeed, T. Bouwmans, and S. K. Jung, "Moving object detection in complex scene using spatiotemporal structured-sparse RPCA," *IEEE Trans. Image Process.*, vol. 28, no. 2, pp. 1007–1022, Feb. 2019.
- [31] B. Shen, W. Xie, and Z. J. Kong, "Smooth robust tensor completion for background/foreground separation with missing pixels: Novel algorithm with convergence guarantee," *J. Mach. Learn. Res.*, vol. 23, no. 217, pp. 1–40, Jul. 2022.
- [32] B. Shen, R. R. Kamath, H. Choo, and Z. Kong, "Robust tensor decomposition based background/foreground separation in noisy videos and its applications in additive manufacturing," *IEEE Trans. Autom. Sci. Eng.*, vol. 20, no. 1, pp. 583–596, 2023.
- [33] R. Rubinstein, A. M. Bruckstein, and M. Elad, "Dictionaries for sparse representation modeling," *Proc. IEEE*, vol. 98, no. 6, pp. 1045–1057, 2010.
- [34] H. Bristow, A. Eriksson, and S. Lucey, "Fast convolutional sparse coding," in *Proc. IEEE Conf. Comput. Vis. Pattern Recognit. (CVPR)*, June 2013, pp. 391–398.

- [35] B. Wohlberg, "Efficient convolutional sparse coding," in *Proc. IEEE Int. Conf. Acoust., Speech Signal Process. (ICASSP)*, 2014, pp. 7173–7177.
- [36] B. Wohlberg, "Efficient algorithms for convolutional sparse representations," *IEEE Trans. Image Process.*, vol. 25, no. 1, pp. 301–315, Jan. 2016.
- [37] C. Garcia-Cardona and B. Wohlberg, "Convolutional dictionary learning: A comparative review and new algorithms," *IEEE Trans. Comput. Imag.*, vol. 4, no. 3, pp. 366–381, Sep. 2018.
- [38] C. David, V. Gui, and F. Alexa, "Foreground/background segmentation with learned dictionary," in *Proc. 3rd Int. Conf. Appl. Math., Simulation, Modelling, Circuits, Syst. Signals (ASMCSS)*, 2009, pp. 197–201.
- [39] C. Zhao, X. Wang, and W.-K. Cham, "Background subtraction via robust dictionary learning," *EURASIP J. Image Video Process.*, vol. 2011, pp. 1–12, 2011.
- [40] A. Staglianò, N. Noceti, A. Verri, and F. Odone, "Online space-variant background modeling with sparse coding," *IEEE Trans. Image Process.*, vol. 24, no. 8, pp. 2415–2428, 2015.
- [41] P. Dong, S. Wang, Y. Xia, D. Liang, and D. D. Feng, "Foreground detection with simultaneous dictionary learning and historical pixel maintenance," *IEEE Trans. Image Process.*, vol. 25, no. 11, pp. 5035–5049, 2016.
- [42] J. Wright, Y. Ma, J. Mairal, G. Sapiro, T. S. Huang, and S. Yan, "Sparse representation for computer vision and pattern recognition," *Proc. IEEE*, vol. 98, no. 6, pp. 1031–1044, 2010.
- [43] Z. Zhang, Y. Xu, J. Yang, X. Li, and D. Zhang, "A survey of sparse representation: Algorithms and applications," *IEEE Access*, vol. 3, pp. 490–530, 2015.
- [44] T. Pock and A. Chambolle, "Diagonal preconditioning for first order primal-dual algorithms in convex optimization," in *Proc. Int. Conf. Comput. Vis. (ICCV)*, Nov. 2011, pp. 1762–1769.
- [45] K. Naganuma and S. Ono, "Variable-wise diagonal preconditioning for primal-dual splitting: Design and applications," *IEEE Transactions on Signal Processing*, vol. 71, pp. 3281–3295, 2023.
- [46] A. Beck and T. M., "A fast iterative shrinkage-thresholding algorithm for linear inverse problems," *SIAM J. Imag. Sci.*, vol. 2, no. 1, pp. 183–202, 2009.
- [47] K. Naganuma and S. Ono, "Cross-frame foreground structural similarity modeling by convolutional sparse representation," in *Proc. APSIPA Ann. Summit Conf. (APSIPA ASC)*, 2023, pp. 779–783.
- [48] Y. Xu and W. Yin, "A block coordinate descent method for regularized multiconvex optimization with applications to nonnegative tensor factorization and completion," *SIAM J. Imag. Sci.*, vol. 6, no. 3, pp. 1758–1789, 2013.
- [49] L. Condat, "Fast projection onto the simplex and the l_1 ball," *Math. Program.*, vol. 158, no. 1, pp. 575–585, Jul. 2016.
- [50] M. Afonso, J. Bioucas-Dias, and M. Figueiredo, "An augmented Lagrangian approach to the constrained optimization formulation of imaging inverse problems," *IEEE Trans. Image Process.*, vol. 20, no. 3, pp. 681–695, Mar. 2011.
- [51] G. Chierchia, N. Pustelnik, J.-C. Pesquet, and B. Pesquet-Popescu, "Epigraphical projection and proximal tools for solving constrained convex optimization problems," *Signal, Image Video Process.*, vol. 9, no. 8, pp. 1737–1749, 2015.
- [52] S. Ono and I. Yamada, "Signal recovery with certain involved convex data-fidelity constraints," *IEEE Trans. Signal Process.*, vol. 63, no. 22, pp. 6149–6163, Nov. 2015.
- [53] S. Ono, "Primal-dual plug-and-play image restoration," *IEEE Signal Process. Lett.*, vol. 24, no. 8, pp. 1108–1112, Aug. 2017.
- [54] S. Ono, "Efficient constrained signal reconstruction by randomized epigraphical projection," in *Proc. IEEE Int. Conf. Acoust., Speech and Signal Process. (ICASSP)*, 2019, pp. 4993–4997.
- [55] K. Naganuma and S. Ono, "A general destriping framework for remote sensing images using flatness constraint," *IEEE Trans. Geosci. and Remote Sens.*, vol. 60, pp. 1–16, Feb. 2022, art no. 5525016.
- [56] K. Sato and S. Ono, "Towards robust hyperspectral anomaly detection: Decomposing background, anomaly, and mixed noise via convex optimization," *arXiv:2401.14814*, 2024. [Online]. Available: <https://arxiv.org/abs/2401.14814>
- [57] K. Naganuma and S. Ono, "Toward robust hyperspectral unmixing: Mixed noise modeling and image-domain regularization," *IEEE J. Sel. Topics Appl. Earth Observ. Remote Sens.*, vol. 17, pp. 8117–8138, 2024.
- [58] S. Takemoto and S. Ono, "Spatio-spectral structure tensor total variation for hyperspectral image denoising and destriping," *arXiv:2404.03313*, 2024.
- [59] K. Naganuma and S. Ono, "Static-scene constrained optimization for matrix/tensor-decomposition-free foreground-background separation," in *Proc. IEEE Int. Conf. Acoust., Speech and Signal Process. (ICASSP)*, 2023, pp. 1–5.
- [60] E. Gebhardt and M. Wolf, "CAMEL dataset for visual and thermal infrared multiple object detection and tracking," in *Proc. IEEE Int. Conf. Adv. Video Signal Based Surveill. (AVSS)*, 2018, pp. 1–6.
- [61] P. Saha, B. A. Mudassar, and S. Mukhopadhyay, "Adaptive control of camera modality with deep neural network-based feedback for efficient object tracking," in *Proc. IEEE Int. Conf. Adv. Video Signal Based Surveill. (AVSS)*, 2018, pp. 1–6.
- [62] AntiUAV 9 Aniket, "bird dataset," <https://universe.roboflow.com/antiuav-9-aniket/bird-6le8u>, jun 2022, visited on 2024-07-27. [Online]. Available: <https://universe.roboflow.com/antiuav-9-aniket/bird-6le8u>
- [63] O. Riou, S. Berrebi, and P. Bremond, "Nonuniformity correction and thermal drift compensation of thermal infrared camera," in *Proc. SPOE, Thermosense XXVI*, vol. 5405, Apr. 2004, pp. 294–302.
- [64] Z. Wang, A. Bovik, H. Sheikh, and E. Simoncelli, "Image quality assessment: from error visibility to structural similarity," *IEEE Trans. Image Process.*, vol. 13, no. 4, pp. 600–612, Apr. 2004.
- [65] C.-I. Chang, "An effective evaluation tool for hyperspectral target detection: 3D receiver operating characteristic curve analysis," *IEEE Trans. Geosci. Remote Sens.*, vol. 59, no. 6, pp. 5131–5153, 2021.



Kazuki Naganuma (S'21) received a B.E. degree in 2020 from the Kanagawa Institute of Technology and M.E. and Ph.D. degrees in Information and Computer Sciences 2022 and 2024 from the Tokyo Institute of Technology, respectively.

He is an assistant professor at the Institute of Engineering of Tokyo University of Agriculture and Technology. From April 2023 to March 2025, he was a Research Fellow (DC2) of the Japan Society for the Promotion of Science (JSPS). From October 2023 and April 2025 to present, He is a Research Fellow (PD) of JSPS and a Researcher of ACT-X of the Japan Science and Technology Corporation (JST), Tokyo, Japan. His current research interests are in signal and image processing and optimization theory.

Dr. Naganuma received the Student Conference Paper Award from IEEE SPS Japan Chapter in 2023.



Shunsuke Ono (S'11–M'15–SM'23) received a B.E. degree in Computer Science in 2010 and M.E. and Ph.D. degrees in Communications and Computer Engineering in 2012 and 2014 from the Tokyo Institute of Technology, respectively.

From 2012 to 2014, he was a Research Fellow (DC1) of the Japan Society for the Promotion of Science (JSPS). He was an Assistant, then an Associate Professor with Tokyo Institute of Technology (TokyoTech), Tokyo, Japan, from 2014 to 2024. From 2016 to 2020, he was a Researcher of Precursory Research for Embryonic Science and Technology (PRESTO), Japan Science and Technology Agency (JST), Tokyo, Japan. Currently, he is an Associate Professor with Institute of Science Tokyo (Science Tokyo), Tokyo, Japan. His research interests include signal processing, image analysis, optimization, remote sensing, and measurement informatics. He has served as an Associate Editor for IEEE TRANSACTIONS ON SIGNAL AND INFORMATION PROCESSING OVER NETWORKS (2019–2024).

Dr. Ono was a recipient of the Young Researchers' Award and the Excellent Paper Award from the IEICE in 2013 and 2014, respectively, the Outstanding Student Journal Paper Award and the Young Author Best Paper Award from the IEEE SPS Japan Chapter in 2014 and 2020, respectively, and the Best Paper Award in APSIPA ASC 2024. He also received the Funai Research Award in 2017, the Ando Incentive Prize in 2021, the MEXT Young Scientists' Award in 2022, and the IEEE SPS Outstanding Editorial Board Member Award in 2023.